Simulating neutron stars with a flexible enthalpy-based equation of state parametrization in SpECTRE

Isaac Legred,[1, 2] Yoonsoo Kim,[1, 3] Nils Deppe,[3] Katerina Chatziioannou,[1, 2]
Francois Foucart,[4] François Hébert,[3] and Lawrence E. Kidder[5]

[1]*Department of Physics, California Institute of Technology, Pasadena, California 91125, USA*
[2]*LIGO Laboratory, California Institute of Technology, Pasadena, California 91125, USA*
[3]*Theoretical Astrophysics 350-17, California Institute of Technology, Pasadena, CA 91125, USA*
[4]*Department of Physics & Astronomy, University of New Hampshire, 9 Library Way, Durham NH 03824, USA*
[5]*Cornell Center for Astrophysics and Planetary Science, Cornell University, Ithaca, New York 14853, USA*

Numerical simulations of neutron star mergers represent an essential step toward interpreting the full complexity of multimessenger observations and constraining the properties of supranuclear matter. Currently, simulations are limited by an array of factors, including computational performance and input physics uncertainties, such as the neutron star equation of state. In this work, we expand the range of nuclear phenomenology efficiently available to simulations by introducing a new analytic parametrization of cold, beta-equilibrated matter that is based on the relativistic enthalpy. We show that the new *enthalpy parametrization* can capture a range of nuclear behavior, including strong phase transitions. We implement the enthalpy parametrization in the SpECTRE code, simulate isolated neutron stars, and compare performance to the commonly used spectral and polytropic parametrizations. We find comparable computational performance for nuclear models that are well represented by either parametrization, such as simple hadronic EoSs. We show that the enthalpy parametrization further allows us to simulate more complicated hadronic models or models with phase transitions that are inaccessible to current parametrizations.

I. INTRODUCTION

Multimessenger observations of the gravitational wave event GW170817 [1, 2] have highlighted the role of neutron star binaries (BNS) in probing the physics of dense matter, e.g., [3–5]. In addition, further astronomical observations [1, 6–13] and terrestrial nuclear experiments [14, 15] have facilitated new insights into the equation of state (EoS) of NS matter [9, 10, 16–22]. Nonetheless significant uncertainty exists about the properties of dense matter above nuclear saturation density[1], $\rho_{\rm nuc} \equiv 2.8 \times 10^{14} {\rm g/cm}^3$, which translates to uncertainty in the properties of astrophysical NSs whose densities can reach $\sim 7\rho_{\rm nuc}$ [18, 22].

The merger phase of a BNS coalescence carries the largest imprint of nuclear matter and strong gravity and it can only be studied numerically. Numerical relativity (NR) simulations of BNS coalescences through merger require solving the equations of general relativistic magnetohydrodynamics (GRMHD) simultaneously with the Einstein field equations and, possibly, the Boltzmann equations for neutrino radiation transport [24–26]. The system of equations is closed with a nuclear EoS. See e.g. [27–31] for reviews of the field. Such simulations have been used to interpret existing signals, e.g. [32–37], and targeted simulations will likely be an essential tool for understanding future observations.

The most generic strategy for representing the nuclear EoS numerically is piecewise, i.e., using independent expressions in different density or pressure intervals. For example, interpolated tables of thermodynamic quantities such as pressure and internal energy at every value of the density and composition offer access to the widest range of nuclear behavior. However, the temperature- and composition-dependent tables currently used, e.g. [38], have a significant memory footprint and evaluation requires computationally expensive operations such as constant access to the table and interpolation [39]. The latter may also be inaccurate (at low order) or prone to unphysical oscillations for EoSs with discontinuities or underresolved features (at high order). A related approach makes use of piecewise parametrizations such as a *piecewise-polytrope* [40], which is effectively a sparsely sampled table for the polytropic exponent. Though it can capture a range of high-density behavior, discontinuities in derivatives of thermodynamic quantities can degrade simulation accuracy [41, 42].

A different strategy is based on functional representations of the EoS that stay smooth across density scales, such as a *single-polytropic* or *spectral* parametrization [41–44]. Such parametrizations typically cannot fully represent nuclear EoS models, as they are restricted to a finite number of parameters in the density range of interest [41, 44]. On top of this, smoothness across density scales fails to capture nuclear models that contain nuclear transitions to exotic degrees of freedom.

In this study, we propose a new parametrization of the nuclear EoS that bridges smooth and discontinuous models while balancing accuracy and computational efficiency.[2] We parametrize the relativistic enthalpy [45] via

---

[1] The saturation density of atomic nuclei is determined via theory and experiments [23]; here we fix a value for convenience.

[2] We use the term "model" to refer to a nuclear-theoretic predic-

a combination of analytic polynomials and trigonometric functions. Unlike pressure, the difference in enthalpy at densities $[\rho_{\mathrm{nuc}}, 3\rho_{\mathrm{nuc}}]$ for two EoSs is typically small compared to the enthalpy of either. The enthalpy can thus be effectively written as a "baseline" part plus small corrections. We capitalize on this in order to write the enthalpy as a polynomial, typically capturing $\sim 99\%$ of the EoS, plus small trigonometric corrections, bringing the fit accuracy to 1 in 10^5. Such a decomposition can capture a wide range of phenomenology with modest changes to the relevant parameters. In addition, further thermodynamic quantities such as the pressure can be evaluated efficiently and analytically.

We implement this parametrization in SpECTRE [46, 47], a scalable next-generation multiphysics computational astrophysics code that uses task-based parallelism [48]. A primary science target for SpECTRE is fast and accurate GRMHD simulations of BNS coalescences. We use SpECTRE to test the *enthalpy parametrization* on isolated NSs in the Cowling approximation, i.e. we do not evolve the spacetime [49], while evolving the ideal GRMHD equations [26] with a discontinuous Galerkin-finite difference (DG-FD) hybrid scheme [50, 51]. Though these simulations assume a static spacetime, they still allow us to evaluate the role of the enthalpy parametrization in questions of convergence, efficiency, and resolvability of nuclear physics in simulations.

We show that the enthalpy parametrization is able to effectively represent a wide range of nuclear behavior, while incurring small additional computational costs relative to simpler parametrizations. After reviewing the general requirements a parametrization must meet in Sec. II, we introduce the enthalpy parametrization in Sec. III. We demonstrate that it can faithfully fit nuclear models ranging from constant-speed-of-sound models, polytropes, and phase transitions in Secs. III B and V, to smooth EoSs in Secs. IV and V. We perform numerical simulations with SpECTRE and find that for resolutions of at least $130\,\mathrm{m}$, the EoS evaluation cost is subdominant to other simulation components. We simulate hybrid stars with quark cores in Sec. V C, and find that such simulations can be carried out stably with better-than-expected runtime scaling properties under increasing resolution.

II. EOS PARAMETRIZATIONS FOR RELATIVISTIC SIMULATIONS

A. General requirements

We begin with a general discussion of the requirements phenomenological parametrizations of the nuclear EoS must meet for efficient use in numerical simulations. These include (i) faithful representation of target nuclear

---

models, (ii) parametric extensibility, and (iii) computational performance related to smoothness (to the extent allowed by the underlying nuclear physics) and/or a fully analytic formalism.

The first requirement is that the parametrization is generic enough that it can faithfully represent the target nuclear physics. While no standard faithfulness metrics exist, a common test is the L^2 difference of quantities of interest [40, 43]. Nonetheless it is unclear how different metrics relate, for example the L^2 difference of the local polytropic indices and that of the mass-radius curve [41, 52]. One particular challenge to smooth parametrizations is modeling strong phase transitions [53, 54]. In general we would like a parametrization where, whatever the metric, we can improve the fit via iterative approximation. In principle this is available to any parametrization by adding more parameters and smoothly changing parameter values. In practice, however, the functional form of the parametrization may limit the accessible parameter space, as shown in [55] for the spectral parametrization.

The second requirement is that the parametrization allows us to parametrically explore a wide range of possible high-density behavior. This entails continuously, and without significant fine-tuning, extending the parametrization to produce EoSs that might differ from existing nuclear models. An example of such an extension would be a parameter which controls the pressure at a particular density and thus allows us to isolate the effect of this density scale on macroscopic observables. Another benefit of such continuous extensibility is that it allows us to construct a map from the EoS to observables. This approach has already been successfully used in the case of binary black hole mergers to produce accurate *surrogates* of the map of binary configurations to gravitational waves [56, 57]. A similar methodology could be used to construct a surrogate for the post-merger gravitational-wave signature of BNS mergers, whose EoS dependence is not well captured by a small number of parameters [58, 59].

At the same time, we consider practical requirements in terms of computational performance: speed and accuracy of the relevant evaluations, and smoothness of the thermodynamic quantities where possible. A fully analytic form for the EoS and all the relevant thermodynamic quantities is a sufficient (but perhaps not necessary) condition. Tabulated EoSs, while guaranteeing maximal flexibility, fail in this regard. Consider, for example, primitive variable recovery. Numerical simulations evolve the components of the stress-energy tensor which are nonlinear functions of primitive variables such the rest-mass baryon density ρ, pressure p, and specific internal energy ϵ. This process involves inverting the relation between the stress-energy tensor and the primitive variables with root-finding routines during which the EoS, for example $p(\epsilon)$, is evaluated repeatedly. For tabulated EoSs this includes computing the temperature T from ϵ via another root-find and then computing $p(T)$

---

via a table lookup and interpolation. The EoS tables are typically too large to store in the CPU caches and so the nested root-finding routines require repeated loading of data from main memory, causing significant overhead that dominates simulation cost [39].

Another advantage of fully analytical parametrizations is that they enable efficient computation of all necessary thermodynamic quantities in a consistent way. Besides tabulated EoSs, this also applies to certain parametrizations that require interpolation or numerical integration. For example, the spectral parametrization allows for analytic evaluation but not integration of $d\epsilon/d\rho$. Then, $\epsilon(\rho)$ is computed via a computationally expensive numerical integral as high accuracy is required to avoid thermodynamic inconsistency during primitive variable recovery.

B. Existing parametrizations of the EoS

The simplest parametrization of cold, beta-equilibrated, dense matter is a single polytrope that prescribes a relationship between the rest-mass baryon density ρ and the pressure p

$$p(\rho) = K\rho^\Gamma \,, \tag{1}$$

where Γ is the the polytropic exponent and K is the polytropic constant; both are independent of ρ. For example, a degenerate neutron gas would obey a polytropic relation with $\Gamma = 5/3$. Polytropes have a long history in NS simulations, e.g., [60–63], and more recent code tests, e.g., [51, 64, 65], due to their simplicity, low computational cost, and the fact that they allow for analytic evaluation of pressure, internal energy, specific enthalpy, and rest-mass density. Nonetheless, their simplicity makes polytropes incompatible with realistic EoS nuclear models, either hadronic (for example, polytropes do not satisfy the same universal relations as hadronic models [66]) or hybrid ones that include multiple degrees of freedom.

Piecewise-polytropes [67] extend single-polytropes to multiple polytropic segments at different densities, thereby decoupling low- and high-density behavior. With enough piecewise segments, piecewise-polytropes can also fit EoSs with strong phase transitions [68]. While piecewise-polytropes retain some of the computational simplicity of the single-polytrope and have been employed in BNS mergers [69–72], the lack of smoothness across stitching boundaries tends to increase the computational cost and decrease the accuracy [41, 42]. Extensions to continuous polytropic indices [42, 73] ensure smoothness, but at the cost of additional parameters and a locally non-constant polytropic exponent which could hamper performance. The large number of additional parameters is typical for smooth piecewise representations as one additional parameter is required per transition per degree of differentiability. More formally, in order to smoothly stitch two generic parametrized $\mathcal{C}^\infty$ functions across a transition, $n + 1$ parameters must be matched to obtain a globally $\mathcal{C}^n$ result.

Finally, the spectral parametrization [43] accurately reflects a broad range of nuclear models while maintaining smoothness across density scales. The parametrization has a similar form to a polytrope

$$p(\rho) = K\rho^{\Gamma(\rho)} \,, \tag{2}$$

but now $\Gamma(\rho)$ is expanded in a basis of smooth functions, typically a polynomial. The spectral parametrization can successfully reproduce hadronic nuclear models with a comparable number of parameters as polytropes, though it cannot capture sharp changes in the speed of sound that are associated with phase transitions [41, 43]. Compared to piecewise polytropes and other EoS with discontinuities, the spectral parametrization can lead to reduced computational cost in simulations [41] for a given accuracy requirement, while remaining more computationally intensive than pure polytropes. Our current implementation of the spectral EoS balances faithfulness to nuclear models and computational efficiency by expressing $\Gamma(\rho)$ as a a polynomial in $\log \rho$ [41]. More complex basis functions could improve faithfulness, but they would come at the cost of computational efficiency since computation of the internal energy requires a numeric integral whose accuracy depends on how rapidly $\Gamma(\rho)$ varies.

The above discussion highlights the role of balancing faithfulness and computational efficiency in selecting EoS parametrizations for numerical simulations. While the single-polytrope is computationally efficient, it is too restrictive in terms of nuclear physics. Piecewise-polytropes expand the range of nuclear models accessible, but at the cost of longer runtimes and loss of accuracy due to non-smoothness at the stitching boundaries. The spectral parametrization strikes some balance, but performs optimally when few parameters are used; it is therefore restricted to simple nuclear models. Ultimately, we would prefer an EoS parametrization which is able to fit to a problem-specific precision, matching the level of other errors in simulations at the lowest possible cost. This motivates the introduction of a new parametrization with increased flexibility to model a wider range of nuclear EoSs without considerable performance losses.

III. ENTHALPY PARAMETRIZATION OF THE EOS

In this section we introduce a new *enthalpy parametrization* with a flexible number of degrees of freedom that expands the range of microscopic physics we are able to represent in numerical simulations. In the following, we work in geometric units: $c = 1$, $G = 1$.

A. Parametrizing the enthalpy

The specific enthalpy of a system h is defined as the enthalpy per unit mass. In relativistic contexts it represents the energy required to inject a unit of rest mass

into the system while remaining in thermodynamic equilibrium. The first law of thermodynamics requires that at zero temperature T and in β−equilibrium,

$$h(\rho) \equiv \left(\frac{\partial e}{\partial \rho}\right)_{T,\beta} = \frac{de}{d\rho} = \frac{p(\rho) + e(\rho)}{\rho}\,, \qquad (3)$$

where e and p are the energy density and pressure, while ρ is the rest-mass energy density of baryons.

We choose to directly parameterize the enthalpy for three primary reasons. First, the enthalpy is a monotonically-increasing and slowly-varying function of the baryon density, which is numerically beneficial. Second, the enthalpy can be intuitively interpreted as a measure of the stiffness of the EoS: a larger enthalpy corresponds to higher pressure and energy density. Third, and importantly for hydrodynamic simulations, the enthalpy in cold, beta-equibrilated matter is related to other thermodynamic quantities by linear operations, which facilitates analytic calculations and avoids interpolation or numerical integration.

From the first law, we have

$$\frac{dh}{d\log\rho} = \frac{de}{d\rho} + \frac{dp}{d\rho} - h = \frac{dp}{d\rho} = \frac{dp}{de}\frac{de}{d\rho} = hc_s^2\,, \qquad (4)$$

and

$$\frac{dp}{d\rho} = \frac{dh}{d\log\rho}\,, \qquad (5)$$

$$\frac{dh}{d\log\rho} = hc_s^2\,. \qquad (6)$$

Equation (5) suggests that $dp/d\rho$ is zero if and only if $dh/d\rho$ is zero. Equation (6) provides the motivation for our parametrization choices. Consider, for example, a constant speed of sound $c_s = c_{s,0}$. Then

$$c_{s,0}^2 = c_s^2 = \frac{dp}{de} \implies p = p_0 + c_{s,0}^2 \Delta e\,, \qquad (7)$$

with $p_0 = p(e_0)$ and $\Delta e \equiv e - e_0$. In this special case Eq. (6) becomes

$$h(\log\rho) \propto \exp\left(c_{s,0}^2 \log\rho\right)$$
$$\approx \rho_0\left[1 + c_{s,0}^2 \log\left(\rho/\rho_0\right) + \dots\right]\,, \qquad (8)$$

where ρ_0 is some fiducial density. Equation (8) suggests that if c_s^2 is slowly varying,[3] the enthalpy can be approximated as exponential in $\log\rho$. Moreover, a smaller c_s^2 accelerates the convergence of the series of Eq. (8), though this also depends on the choice of density scale ρ_0. We therefore choose the Taylor expansion in Eq. (8) as the starting point of the enthalpy parametrization.

We further select $\log\rho/\rho_0$, as the independent variable of the parametrization. This choice enables us to better

_____

[3] In general, causality and stability bound $0 \leq c_s^2 \leq 1$.

resolve the low-density EoS. Equation (8) further suggests that $h(\log\rho) \propto \exp(c_{s,0}^2 \log\rho)$ is analytically and computationally simpler than $h(\rho) \propto \rho^{c_{s,0}^2}$ as the Taylor expansion of $\rho^{c_{s,0}^2}$ converges more slowly than the expansion of $\exp(c_{s,0}^2 \log\rho)$ for non-integer $c_{s,0}$.

Lastly, a desirable property of the specific enthalpy is that it is continuous across first-order phase transitions. This can be seen from Eq. (5) where maintaining a constant pressure across the transition guarantees that the enthalpy will be constant as well. This indicates that across certain weak transitions the enthalpy can be expanded in a basis of continuous functions, unlike, for example, a local polytropic exponent.

B. Decomposition

Motivated by Eq. (8), we introduce a parametrization of $h(\log\rho)$. Given an EoS in some density region $\rho_{\min} \leq \rho \leq \rho_{\max}$ we select a density scaling parameter $\rho_0 \leq \rho_{\min}$ such that $z \equiv \log(\rho/\rho_0)$ is positive in the relevant density range. Importantly, ρ_0 is not necessarily equal to $\rho_{\min}$ thus introducing an additional parameter. We then write

$$h(z) \approx h_p(z) \equiv \sum_{i=0}^{i_{\max}} \gamma_i z^i\,, \qquad (9)$$

where $h(z)$ is the target enthalpy and $h_p(z)$ is its approximation. This polynomial decomposition is motivated by the previous observation that $h(z)$ is approximately exponential in z for nearly constant speeds of sound, corresponding to $\gamma_i \sim c_{s,0}^{2i}/i!$. The rapid convergence of the γ_i sequence indicates that the $i > i_{\max}$ terms will be small provided that the speed of sound is slowly varying.

Given that $h(z)$ is positive and increasing and $z_i > 0$, catastrophic floating point cancellation in numerical calculations can be avoided by restricting to $\gamma_i \geq 0$. This guarantees that each term $\gamma_i z^i$ is a small and positive correction to previous terms. Furthermore, the polynomial expansion of Eq. (9) can be efficiently and stably evaluated with Horner's method [74]. Allowing for more general γ_i is possible, but this comes at a risk of oscillatory behavior and cancellation of large terms which make convergence predictions difficult. The implications and rationale behind the choice to set $\gamma_i \geq 0$ are further discussed in App. C.

A consequence of setting $\gamma_i \geq 0$ is that Eq. (9) is unable to model certain EoSs, for example the case where $dh/dz = hc_s^2$ is not strictly increasing, even with $i_{\max} \to \infty$. Such a non-monotonic speed of sound could be encountered for complicated hadronic models or more generically if non-hadronic degrees of freedom are introduced [75]. We therefore augment Eq. (9) by decomposing $h_t(z) \approx h(z) - h_p(z)$ as a Fourier series

$$h_t(z) \equiv \sum_{j=1}^{j_{\max}} a_j \sin(jkz) + b_j \cos(jkz)\,, \qquad (10)$$

where k sets the "wavelength scale" of the fit. In a Fourier series k is typically fixed to

$$k = k_F \equiv \frac{2\pi}{z_{\max} - z_{\min}} = \frac{2\pi}{\log(\rho_{\max}/\rho_{\min})} \,, \qquad (11)$$

but here we vary it and find that $k \gtrsim k_F$ leads to good fits. The effect of perturbing k around k_F is small, as we explore in App. A. The trigonometric expansion of Eq. (10) can also serve as a low-pass filter to remove high-frequency oscillations from the tabulated EoS data that may not be physical or computationally resolvable. In summary, the enthalpy parametrization is

$$h_*(z) \equiv h_t(z) + h_p(z) \approx h(z) \,. \qquad (12)$$

In Fig. 1 we demonstrate the enthalpy parametrization fit of Eq. (12) and its polynomial, Eq. (9), and trigonometric, Eq. (10), components for a phenomenological EoS drawn from a Gaussian process prior [76, 77]. The polynomial fit alone is accurate to about $\mathcal{O}(1\%)$, while the total fit is good to about one part in 10^5. For reference, we also plot $c_s^2 = (1/h)dh/dz$, as a measure of the complexity of the EoS. Even though c_s^2 is not globally nearly constant, it is slowly varying and nearly monotonic.

Given the generic form of the enthalpy parametrization, there is no guarantee that a particular fit will satisfy stability $c_s^2 \geq 0$ and causality $c_s^2 \leq 1$. If $h_t(z) = 0$, the fit is guaranteed to be stable, and a sufficient but not necessary condition for causality is $\gamma_i \leq \gamma_{i-1}/i$, which becomes necessary and sufficient in the case of a constant sound speed. If $h_t(z)$ is nonzero, then both conditions must be checked on a grid of spacing

$$\delta z \lesssim \frac{z_{\max} - z_{\min}}{j_{\max}k} \,, \qquad (13)$$

where, as above, $j_{\max}$ is the index of the fastest varying "Fourier" mode. While an unstable fit to the EoS cannot be tolerated in a numerical simulation, an acausal fit may be used if it is very nearly causal (i.e. if $\sqrt{c_s^2 - 1}$ is small compared to the velocity resolution of the simulation). In practice, however, fits typically are neither acausal nor unstable; if they are it is often a sign that the fit to the EoS is poor and more parameters should be used.

C. Computing thermodynamic quantities

Given the expansion of Eq. (12), we can analytically compute the thermodynamic quantities needed for GRMHD evolution as formulated in SpECTRE [46, 51], or similar codes [78]. For example, the energy density is

$$\frac{de}{dz} = \rho \frac{de}{d\rho} = \rho_0 \exp(z) h(z) \Rightarrow$$
$$e(z) = \rho_0 \int_{z_0}^{z} \exp(z') h(z') dz' + e(z_0) \,. \qquad (14)$$

Since $h(z)$ is expressed in terms of sines, cosines, and polynomials, the integral of Eq. (14) can be computed using the following identities

$$\int \exp(z) \sin(nkz) dz$$
$$= \exp(z) \frac{\sin(nkz) - nk\cos(nkz)}{1 + n^2k^2} + C \,, \qquad (15)$$
$$\int \exp(z) \frac{z^n}{n!} dz$$
$$= \exp(z) \frac{z^n}{n!} - \int \frac{z^{n-1}}{(n-1)!} \exp(z) dz = \dots \,, \qquad (16)$$

where the ellipses indicate that integration by parts can be repeated until the integral becomes trivial. Equation (16) is also a gamma function, but it is typically incomplete. Nonetheless, all integrals can be evaluated analytically and $e(z)$ has an expansion of the form

$$e(z) = \exp(z) \times$$
$$\left(\sum_i c_i' z^i + \sum_j a_j' \sin(kjz) + b_j' \cos(kjz) \right)$$
$$+ e_* \,, \qquad (17)$$

where the constant e_* is determined by setting $e(z_{\min}) = e_{\min}$ and the coefficients satisfy

$$\gamma_i' = \frac{1}{i!} \sum_{i_{\max} \geq \ell \geq i} (-1)^{i_{\max} - \ell} \ell! \gamma_\ell \,, \qquad (18)$$
$$a_j' = \frac{a_j}{1 + j^2k^2} + \frac{b_j jk}{1 + j^2k^2} \,, \qquad (19)$$
$$b_j' = \frac{b_j}{1 + j^2k^2} - \frac{a_j jk}{1 + j^2k^2} \,. \qquad (20)$$

The pressure $p(z)$ can also be evaluated analytically with a similar expansion given that

$$p(z) = \rho_0 h(z) \exp(z) - e(z) = h\rho - e \,. \qquad (21)$$

This equation showcases the benefits of setting $\gamma_i \geq 0$ in Eq. (9) to avoid cancellations in the enthalpy expansion. The pressure is computed as the difference of two relatively large quantities, each typically 1–3 orders of magnitude larger than the pressure itself in the relevant density interval. If the expansion of $h(z)$ additionally had large coefficients (i.e. much larger than the enthalpy) terms of $e(z)$ will be computed by sums of alternating large numbers, which is numerically undesirable. However, because $\gamma_\ell \sim 1/\ell!$ for EoSs with slowly varying speed of sound, the terms in Eq. (18) are of comparable size, and about the same size as corresponding terms of $h(z)$. Thus the terms of $p(z)$ are computed to comparable precision as the terms of $e(z)$ and $h(z)$. We find this holds more broadly, even when the speed of sound is not slowly varying, as γ_ℓ is typically decreasing even if it is not decreasing exponentially as in the constant-c_s^2 case.
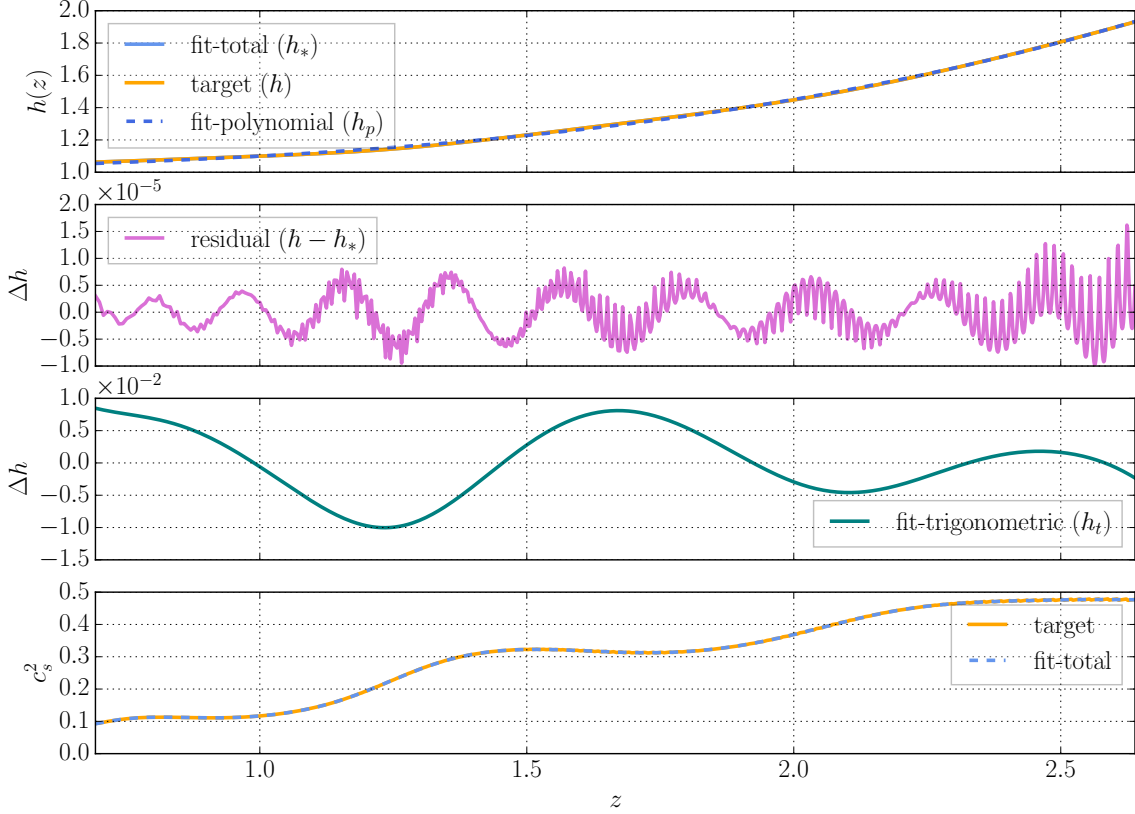
Figure 1. Results of a fit to an EoS drawn from a Gaussian process with the enthalpy parametrization. We plot various thermodynamic quantities as a function of z. The fit parameters are $\rho_{\min} = \rho_{\mathrm{nuc}}$, $\rho_0 = 0.5\rho_{\mathrm{nuc}}$, $k = \pi/(\log(7))$, and $i_{\max} = j_{\max} = 10$. *Top Panel:* The tabulated EoS h (solid, orange) and the total fit h_* (solid, light blue). We also plot the polynomial fit to the EoS h_p (dashed, indigo). Both the total and the polynomial fit are indistinguishable from the tabulated EoS by eye. *Second Panel:* The residuals of the total fit $h - h_*$. *Third Panel:* The trigonmetric fit $h_r = h - h_p$. *Fourth Panel:* $(1/h)dh/dz = c_s^2$, for both the tabulated EoS and the total fit. Throughout we find excellent agreement.

Lastly, we can also analytically compute

$$\frac{dp}{d\rho} = \frac{dh}{dz}, \tag{22}$$

through

$$\frac{dh}{dz} = \sum_i i\gamma_i z^{i-1}$$
$$+ \sum_j jk \left[a_j \cos(jkz) - b_j \sin(jkz) \right] . \tag{23}$$

As can be seen from Eqs. (17) and (23), parameters that enter linearly in the original expansion of $h(z)$ also appear linearly in all relevant thermodynamic quantities.

D. Low-Density Stitching

The enthalpy parametrization is best suited for high-density regions where pressure and energy density are comparable. Low-density regions with $p \ll h\rho \sim e$ might be better fit by direct parametrizations of the pressure. We therefore combine the enthalpy parametrization with a simpler low-density parametrization below $\rho_{\min}$. Incidentally, this density region coincides with the region of validity of nuclear theory calculations [79–81] and terrestrial experiments [14, 15, 82–84]. The low-density EoS is therefore better constrained and thus there is reduced need for flexibility in the EoS parametrization. Moreover, the low-density EoS has a reduced impact on NS observables, especially if the simulation resolution is low, such that $(dp/dr)\Delta r > \delta p$, where Δr is the grid spacing and δp is the difference induced by EoS mismodeling.

A number of options exist for the low-density EoS, including direct parametrizations of nuclear models [79] or chiral effective field theory results [18, 85]. Here we select the existing spectral parametrization implementation [41], as it is more flexible than single-polytropes, but smoother than piecewise-polytropes and tabulated

EoSs. In certain cases, we explore extending the spectral parametrization up to relatively high densities $\sim 2\rho_{\mathrm{nuc}}$ if it can fit the target EoS well-enough in this density regime. Due to the low number of parameters in the spectral parametrization, all degrees of freedom are determined by requiring differentiability of the pressure at the stitching points. We verify this stitching maintains $\mathcal{C}^1$ smoothness, see App. A.

E. Use cases

The requirements laid out in Sec. II are tailored for a specific application of EoS parametrizations, namely numerical simulations involving NSs. These requirements are domain specific and need not necessarily lead to efficient parametrizations for different applications, for example EoS inference using astrophysical data. Besides the general faithfulness and computational efficiency considerations, EoS parametrizations employed in inference need to satisfy an additional requirement: they must provide a reliable path from the observed data to the EoS constraints. Specifically, the data must be the primary driver of inference while the impact of the EoS parametrization itself must be either minimal or driven by first principles and nuclear theory. Parametrizations that impose a functional form for the EoS in terms of a finite number of parameters may fail this requirement. Specifically, the spectral, piecewise-polytropic, and speed-of-sound parametrizations impose additional phenomenological correlations between different densities that are not guided by nuclear theory but instead by the arbitrary functional form of the parametrization itself [86]. Though we have not repeated the analysis of [86], we expect that the enthalpy parametrization has the same pitfall as it possesses many nearly-irrelevant degrees of freedom that are not constrained by current observations and will generically impart correlations between density scales. We therefore caution against using it for inference purposes.

IV. PARAMETRIZATION VERIFICATION

We begin by examining the performance of the enthalpy parametrization for simple nuclear models. Such models can also be expressed with existing parametrizations, providing us with a way to verify the enthalpy implementation and test its impact on computational performance. We use an EoS that is already expressed via the spectral parametrization: SLy1.35 [41], a spectral fit to the SLy EoS [40, 87] with a low-density polytropic exponent of 1.35962.
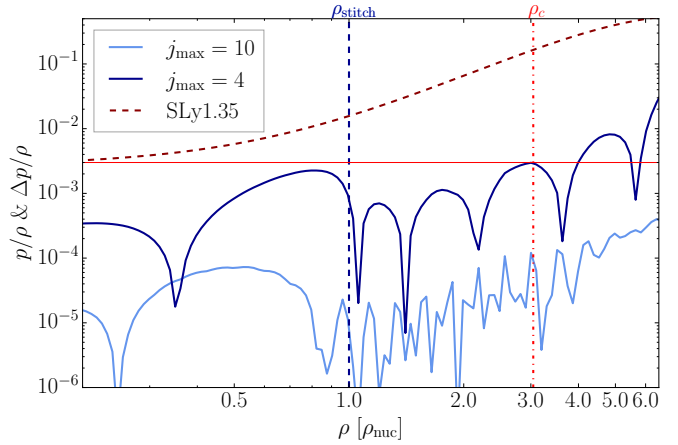

Figure 2. Fitting SLy1.35 (a spectral model of SLy) with the enthalpy parametrization, expressed through the difference in pressure divided by the density. The SLy1.35 EoS value for $p(\rho)/\rho$ is marked by a maroon dashed line for comparison to the residuals. The $j_{\max} = 10$ and $j_{\max} = 4$ fit residuals are marked in light blue and indigo. The vertical blue dashed line marks the stitching density between the enthalpy and the spectral parametrizations, while the vertical red dot-dashed line marks the central density of the NS we simulate in Sec. IV B. The solid red horizontal line marks an error level of 3×10^{-3} for comparison with fits in Sec. V; errors below 3×10^{-3} at $(1, 3)\rho_{\mathrm{nuc}}$ serve as a heuristic for a good fit.

A. SLy1.35: Static tests

We first examine how well the enthalpy parametrization can fit the properties of static NSs. We fit SLy1.35 with the enthalpy parametrization and show the error in pressure divided by density as a function of density in Fig. 2. We vary the number of trigonometric terms in Eq. (10) and show results with $j_{\max} = 10$ and $j_{\max} = 4$. The $j_{\max} = 10$ fit shows exceptional agreement; the error measure, $\Delta p/\rho$, is near or below 1×10^{-4}, which represents sub-percent error over essentially the entire domain. The $j_{\max} = 4$ fit shows increased error, though it remains near or below percent level above ρ_{nuc}. We stitch to a spectral parametrization below ρ_{nuc}, marked in the Fig. 2 as a vertical dashed blue line. Even though the low-density behavior of the EoS is a spectral EoS fitting a spectral EoS, it is not guaranteed the low-density fit is good, because we prioritize smooth stitching to the enthalpy solution above accurate low-density EoS modeling, see App. A. In line with this, we see a significantly better low-density fit for $j_{\max} = 10$.

Fit results on macroscopic NS properties are shown in Fig. 3 where we plot the difference in radius due to the enthalpy fit against the NS gravitational-mass. The $j_{\max} = 10$ fit again shows excellent agreement, with radius error on the order of a few meters for astrophysically relevant NSs. The $j_{\max} = 4$ fit also shows good agreement, with error of order 10 m, smaller than the mismodelling due to the effect of fixing the polytropic exponent
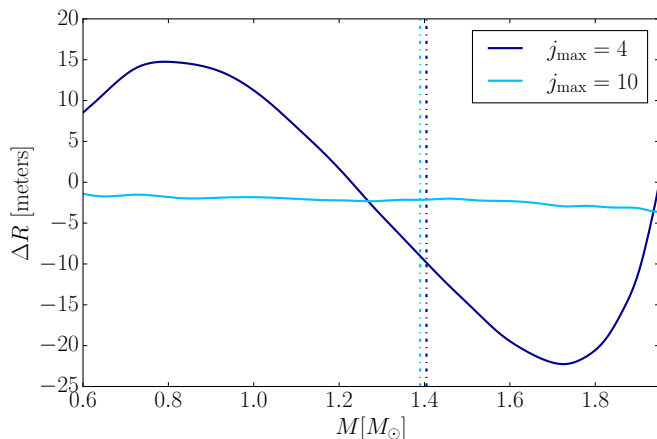
Figure 3. Radius error ΔR as a function of mass for the SLy1.35 EoS and the $j_{max} = 10$ and $j_{max} = 4$ enthalpy parametrization fits. We mark the mass of the stars with central density $\rho_c \sim 3.04\rho_{nuc}$, (simulated in Sec. IV B), with dashed-dot lines. Consistently with the microscopic comparison of Fig. 2, the enthalpy fit can reproduce macroscopic quantities with excellent agreement. The error decreases with more trigonometric terms, but always remains small compared to 200 m grid resolution.

in the crust [41].

B. SLy1.35: Relativistic simulations

We now study the evolution of dynamical NSs using simulations of isolated NSs. As in Ref. [51], we work with SpECTRE within the Cowling approximation and examine NS modes that are sourced by density perturbations due to numerical noise. We neglect spacetime dynamics and magnetic fields, which will likely be most relevant in crust physics where magnetic and matter pressure are comparable. We carry out simulations directly with SLy1.35 using its spectral fit [41] as well as the $j_{max} = 10$ enthalpy parametrization fit; details are given in Table II. We evolve a NS with an initial central density of $\sim 3.04\rho_{nuc}$ which has a Tolman-Oppenheimer-Volkoff (TOV) [88] mass of about $1.4M_\odot$, see Figs. 2 and 3. The simulation resolution corresponds approximately to a 220 m finite difference grid spacing.[4] We plot the central density as a function of time and its spectrum

$$\hat{\rho_c}(\omega) = \int_0^T \rho_c(t)e^{-i\omega t}dt\,, \tag{24}$$

in Fig. 4 and find essentially identical evolution between the spectral and enthalpy fits, in line with expectations from the static tests of Sec. IV A. This demonstrates that

---

[4] We express resolution in finite difference grid spacing for easy comparison to finite difference codes.
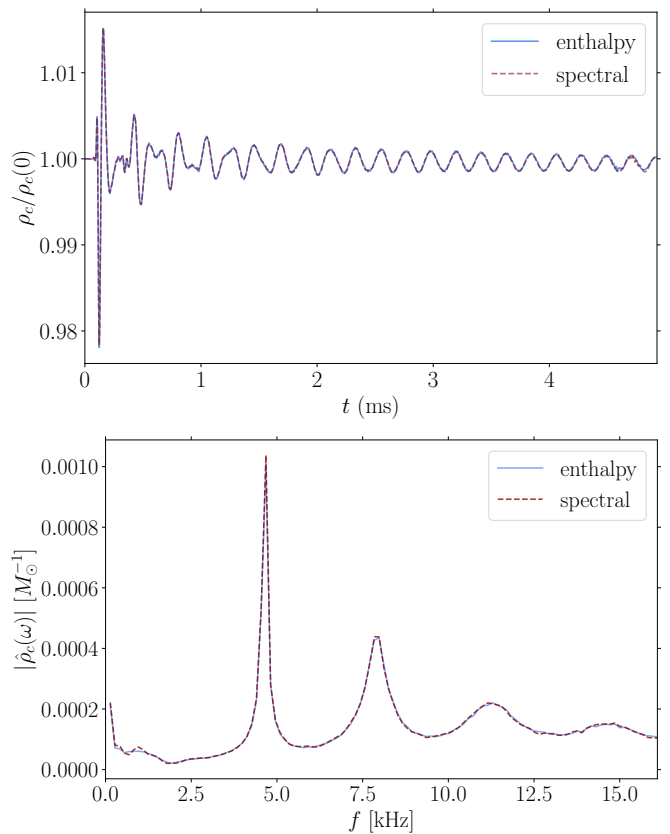

Figure 4. NS central density as a function of time (top panel) and its spectrum (bottom panel) for SpECTRE simulations with SLy1.35 (red dashed) and its $j_{max} = 10$ enthalpy fit (blue solid). These runs are labeled spectral-sly-mc-220 and enthalpy-sly-mc-220 in Table II. In both plots the curves are nearly indistinguishable.

Parametrization	Evaluation Cost (ns) $p(\rho)$	$\epsilon(\rho)$
enthalpy, $j_{max} = 10$	224	225
enthalpy, $j_{max} = 4$	120	120
spectral	62	315

Table I. Evaluation cost in nanoseconds for the spectral and two different enthalpy fits to SLy1.35 for the pressure and internal energy evaluated at $\rho = 5 \times 10^{-4}M_\odot^2$. The spectral parametrization has a shorter (longer) pressure (internal energy) evaluation time. The enthalpy evaluation cost further increases with the number of trigonometric terms employed.

the enthalpy parametrization is able to faithfully reproduce results from lower-dimensional parametrizations.

With regards to computational cost, the enthalpy parametrization results in an overall 15% increase in total runtime compared to the spectral parametrization on similar hardware. To isolate the EoS evaluation cost, we benchmark the $p(\rho)$ and $\epsilon(\rho)$ evaluation in Table I. The two parametrizations have comparable evaluation times though exact numbers are sensitive to the number of trigonometric terms in the enthalpy case. While

$p(\rho)$ evaluation is in general faster with the spectral parametrization, the opposite is true for $\epsilon(\rho)$. This is because the spectral parametrization needs to perform table interpolation to calculate $\epsilon(\rho)$, see Sec. II. In the enthalpy parametrization, trigonometric terms cause slowdowns, although even with $j_{max} = 10$ terms the $p(\rho)$ cost does not exceed a factor of 4. Further studies with single-polytropic nuclear EoSs suggest that this disadvantage effectively disappears if $j_{max} = 0$, see App. B.

V. NUCLEAR MODELS AND PHASE TRANSITIONS

We now turn our attention to more complex nuclear models, including strong phase transitions. We study DBHF [89] and use the constant-speed-of-sound parametrization [90] to construct a model with a strong phase transition, DBHF_2507. We perform static and dynamical tests for both nuclear models. Details about the SpECTRE simulations are given in Table II.

A. DBHF: Fitting a tabulated nuclear model

We fit the tabulated DBHF EoS with the enthalpy parametrization and further explore the effect of low-density stitching to the spectral parametrization by probing two different stitch densities: ρ_{nuc} and $2.5\rho_{nuc}$; these fits are referred to as "low-stitch" and "high-stitch" in what follows. In the high-stitch case we use $j_{max} = 10$ trigonometric terms, while we find that $j_{max} = 5$ is enough for the low-stitch one. See App. A for more details. We examine the microscopic and macroscopic performance of both fits in Figs. 5 and 6. On the microscopic side, the low-stitch fit achieves higher accuracy above $1.1\rho_{nuc}$, but worse accuracy below.

The macroscopic side presents a clearer picture. When we use the enthalpy parametrization to describe the EoS down to a density of ρ_{nuc}, we obtain excellent agreement with the tabulated EoS, with radius differences $\mathcal{O}(1)\,m$ for astrophysically relevant NS masses. However, when we stitch to the spectral parametrization at $2.5\rho_{nuc}$ the radius error increases to $\mathcal{O}(100)\,m$ at $1.4M_\odot$. The improved agreement between the $2.5\rho_{nuc}$ and the ρ_{nuc} stitching fits can be attributed to the high accuracy of the enthalpy parametrization in the range ρ_{nuc} to $2.5\rho_{nuc}$, as seen in Fig. 5. The difference in the two errors is particularly pronounced near $2\rho_{nuc}$, consistent with the observed strong correlation between the pressure at twice saturation density and radius of a $1.4M_\odot$ star [91]. This further establishes the importance of the enthalpy parametrization as a flexible EoS parametrization at nuclear saturation and above, since errors in p/ρ must be at most percent level to achieve high-precision reproduction of astrophysical observables. However, this is not an indication that the spectral parametrization *cannot* fit DBHF well, it just cannot fit DBHF well while
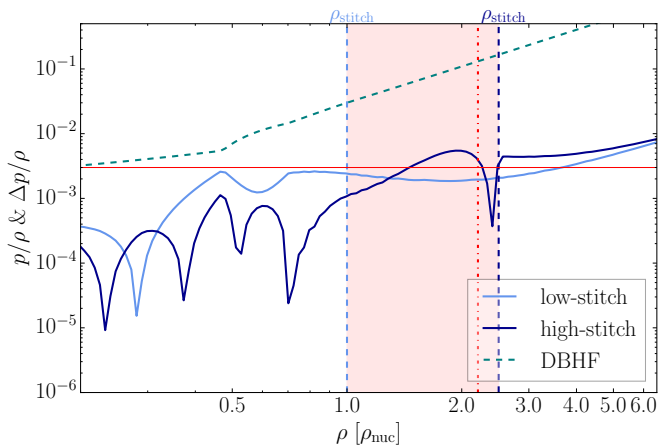

Figure 5. Same as Fig. 2 but for the DBHF nuclear EoS model and two enthalpy fits that are stitched to a spectral parametrization at ρ_{nuc} (low-stitch, light blue) and $2.5\rho_{nuc}$ (high-stitch, indigo). We also plot the tabulated DBHF model $p(\rho)/\rho$ in dashed-teal for reference. The vertical dashed lines denote the stitching densities. We also mark the value $\Delta p/\rho = 3 \times 10^{-3}$ as a solid red horizontal line for reference. We mark the central density of the star we simulate in Sec. V B with a vertical red, dot-dash line.
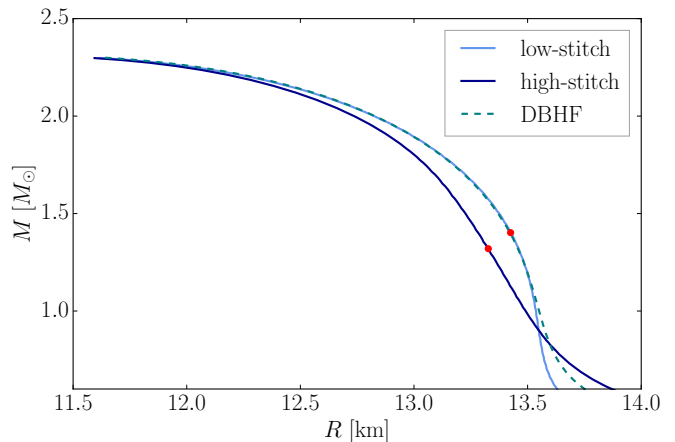

Figure 6. The NS mass-radius relation but for the DBHF nuclear model and two enthalpy fits that are stitched to a spectral parametrization at ρ_{nuc} (low-stitch, light blue) and $2.5\rho_{nuc}$ (high-stitch, indigo). We find visibly improved fits to the M–R relation when the enthalpy parametrization extends down to lower densities. Red dots mark the NSs we evolve in Sec. V B.

maintaining $\mathcal{C}^1$ pressure smoothness at the high-density transition to the enthalpy parametrization and the low density transition to the crust; see App. A.

B. DBHF: Relativistic simulations

We next turn to SpECTRE simulations using the DBHF fits from Sec. V A. Since the low- and high-stitch fits pre-

dict $\mathcal{O}(100)$ m differences for $R_{1.4}$, we target a resolution at that level in order to resolve their effect. We select a NS central density of $2.21\rho_{\rm nuc}$ that lies between the two stitching densities of $\rho_{\rm nuc}$ and $2.5\rho_{\rm nuc}$, see Figs. 5 and 6. Run details and settings are given in Table II. As a consequence, the NS resulting from the high-stitch EoS is fully described by the spectral part of the EoS. In the low-stitch EoS, the NS is described with the enthalpy parametrization out to $r/R \approx 7/8$, about two-thirds of the coordinate volume of the star.

While the high-stitch EoS does represent a spectral fit to the DBHF EoS, the spectral parameters are selected by the requirement that the spectral parametrization reproduces the correct low-density behavior of DBHF and is smoothly stitched to the enthalpy parametrization. It is important to note that a better spectral fit to any particular astrophysical quantity, such as $R_{1.4}$ may be possible, but the fit accuracy is typically lower than in the enthalpy parametrization case. Even if the few degrees of freedom in the spectral model are fit to minimize errors in astrophysical observables, fixing the low-density behavior of the EoS often results in $R(M)$ deviations of 50 m or more [41]. In what follows, we leverage the mismatch of Fig. 6 to examine how well we can resolve EoSs with ~ 100 m radius differences in simulations with similar resolution. Since the high-stitch NS is fully described by the spectral parametrization, this test also serves as a comparison of runtimes between the spectral and enthalpy parametrizations. We do not utilize the tabulated version of DBHF because SpECTRE currently cannot perform GRMHD simulations using tables.

We carry out simulations as detailed in Table II and plot the spectrum of the central density of each star in Fig. 7. The two spectra disagree both in the location of the NS modes and their strength, a consequence of the EoS mismodeling shown in Figs. 5 and 6. In particular, the fundamental radial modes disagree by nearly 3.5%, a difference of ~ 130 Hz in this case. Table II further shows the simulation runtime which is comparable in the 130 m resolution case; each run took about a day on ~ 70 processing elements. Based on the benchmarking results of Sec. IV A, total EoS evaluation time should be comparable for the two runs, as the spectral parametrization evalautes the pressure about twice as quickly as the enthalpy parametrization, but evaluates the internal energy about 3 times slower. Since the number of pressure and internal energy evaluations throughout the entire simulation is not known *a priori*, we cannot preemptively conclude which should run faster, though it is likely the difference would be small. This is reflected in the runtime; differences of 10% are found, with the enthalpy parametrization running slightly faster. Nonetheless, this could be due to an array of confounding factors such as task allocation efficiency, and hardware differences. We therefore conclude that the enthalpy parametrization, despite having more flexibility, is not slower than lower dimensional parametrizations at these resolutions for practical problems.
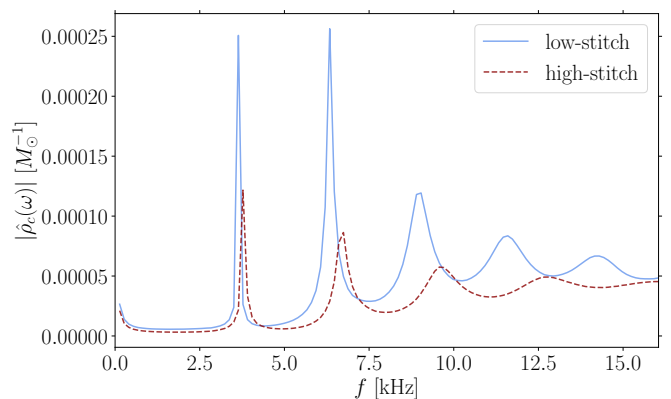

Figure 7. NS central density spectrum for SpECTRE simulations with enthalpy fits to the DBHF nuclear EoS that are stitched to the spectral parametrization at $\rho_{\rm nuc}$ (low-stitch, blue solid) and $2.5\rho_{\rm nuc}$ (high-stitch, red dashed). These runs are labeled enthalpy-dbhf-mc-130 and spectral-dbhf-mc-130 respectively in Table II. The simulated star has a central density of $\approx 2.2\rho_{\rm nuc}$; it is marked in Figs. 5 and 6. In the red case, the NS is completely described by the spectral EoS as its central density is below $2.5\rho_{\rm nuc}$.

C. DBHF_2507: Phase transitions

We now turn our attention to EoS with strong phase transitions and study both smooth and non-smooth (i.e., piecewise) EoSs. We base our studies on DBHF_2507 which is constructed by combining DBHF with the constant-speed-of-sound phenomenological parametrization for strong phase transitions [90]. We select a transition density of $\rho_t = 2.5\rho_{\rm nuc}$ and latent heat ratio $\Delta e/e = 0.7$ [53, 92]. The pressure remains constant during the phase transition, while above that it has a constant speed of sound with $c_s^2 = 1$. The induced phase transition causes a second stable branch to appear in the M–R relation above masses $\sim 1.6 M_\odot$.

1. Piecewise transitions

In its original form described above, DBHF_2507 is piecewise smooth, and it can be represented effectively by a piecewise version of the enthalpy parametrization. Below the phase transition we use either the low- or high-stitch fits from Sec. V, and transition to a new enthalpy segment after the transition. In the high-stitch case, the hadronic part of the EoS is completely described with the spectral parametrization. During the transition, DBHF_2507 possesses a formally constant pressure as a function of density; however, constructing TOV solutions using the method of Lindblom [45] — the TOV method implemented in SpECTRE — requires $dh/dz = dp/d\rho$ to be strictly positive. Therefore, in the transition region we modify the EoS to exhibit $dh/dz = \delta$, where δ is some quantity large enough to guarantee that $h(z)$ is numer-

Table II. Analysis settings for the `SpECTRE` simulations with fits to the SLy1.35, DBHF, DBHF_2507 EoSs, and a polytropic EoS. *Labels* are chosen to serve as unique identifiers for the runs. The integer suffix represents the approximate grid spacing of the run in meters. *Elements* describe the number of computational elements used in the (three-dimensional) domain. *FD Δx* represents the finite-difference grid spacing, in meters, of the finite-difference cells in each element when using finite-difference instead of discontinuous-Galerkin methods; this is the primary measure of resolution of the run and allows for easy comparison to other codes. ρ_c represents the initial central (rest-mass) density of the NS being simulated. *Runtime*, in hours, is the approximate total runtime of each simulation when using *Procs used* processing elements (CPU cores). While runtime depends on an array of factors and may not always be indicative of EoS evaluation speed, differences of $\gtrsim 10\,\mathrm{h}$ on identical settings mark EoS-induced slowdowns. *Figs* represents which figures contain plots pertaining to this run. *Info* represents the section in which more information about the EoS can be found.

Label	Elements	FD Δx (m)	$\rho_c(1/M_\odot^2)$	Runtime (h)	Procs used	Figs	Info
spectral-sly-mc-220	$(24)^3$	224	0.00138	17	138	4	IV
enthalpy-sly-mc-220	$(24)^3$	224	0.00138	20	138	4	IV
spectral-dbhf-mc-130	$(24)^3$	134	0.001	20	138	7	V
enthalpy-dbhf-mc-130	$(24)^3$	134	0.001	18	138	7	V
enthalpy-pt-mc-130	$(24)^3$	134	0.0021	25	138	N/A	V C
enthalpy-pt-ppao-70	$(48)^3$	67	0.0021	119	138	9	V C
enthalpy-pt-mc-70	$(48)^3$	67	0.0021	100	138	9	V C
enthalpy-polytrope-mc-130	$(24)^3$	134	0.00128	20	69	14	B
polytropic-polytrope-mc-130	$(24)^3$	134	0.00128	20	69	14	B

ically invertible, but still small enough to have a small impact on the TOV solution relative to the target resolution.[5] After the end of the phase transition, $h(z)$ is given by a constant speed of sound form, see Eq. (8); this is similar to the procedure demonstrated in [93].

The advantage of the enthalpy parametrization in this problem is that it is able to model constant-speed-of-sound matter (see App. B for the polytropic case) efficiently and with no fine-tuning. Compare this to polytropic (or spectral) models, which can only model constant-speed-of-sound matter well when

$$\Gamma \equiv \frac{\rho}{p}\frac{dp}{d\rho} = \frac{\rho}{p}hc_s^2 = \frac{p+e}{p}c_s^2 \qquad (25)$$

is slowly varying. This is typically not true until some density greater than the phase transition, where $p = p_0 + c_s^2\Delta e \approx c_s^2\Delta e$, especially if c_s^2 is small compared to 1, such as models where $c_s^2 = 1/3$ in the core [94, 95]. In contrast, the enthalpy parametrization can model constant-speed-of-sound matter effectively, and benchmarking results demonstrate that in such cases it can even outperform polytropic EoSs by up to 25%.

We plot the M–R curve in Fig. 8, using the low-stitch and high-stitch fits for the hadronic part of the EoS as discussed in Sec. V A. The low-stitch EoS shows better agreement with DBHF_2507, consistent with previous results; see Fig. 6. The transition mass and radius for the low-stitched model are functionally identical to the tabulated values with errors of $\lesssim 0.01\,M_\odot$ and $\lesssim 1\,\mathrm{m}$. In the high-stitch case the errors increase to $0.05\,M_\odot$ and
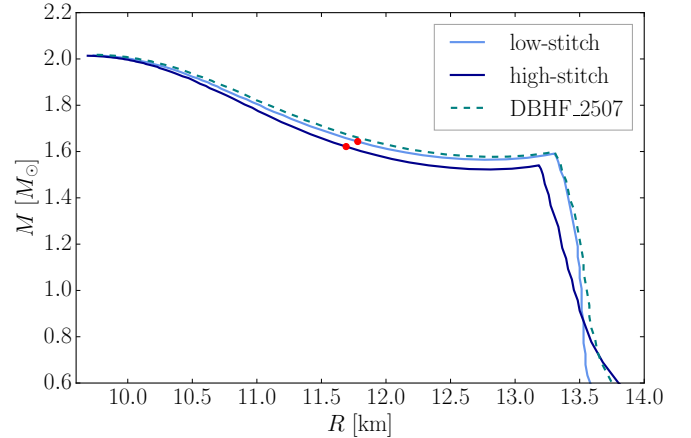

Figure 8. Same as Fig. 6 but for the DBHF_2507 EoS. The procedure by which the low- and high-stitch EoSs of Sec. V A are extended through the phase transition is described in Sec. V C. Consistent with Fig. 6, the low-stitch case can more accurately reproduce the parameters of the phase transition, though caution must be exercised when comparing to tabulated models as differences in interpolation in this case can be substantial. See the text of Sec. V C. As in Fig. 3, red dots mark the NSs we use in subsequent simulations.

$\sim 100\,\mathrm{m}$. Nonetheless, errors decrease with increasing central density and the maximum mass M_{max} is consistent to $\sim 0.01\,M_\odot$ for both fits. This indicates that the enthalpy parametrization can produce effective EoS fits at high densities even when extending a (relatively) poor low-density fit.[6]

---

[5] At a central density of $5.07\rho_{\mathrm{nuc}}$, the difference in radius induced by using $\delta = 1 \times 10^{-4}$ instead of $\delta = 1 \times 10^{-3}$ is less than 5 m.

[6] Such comparisons to tabulated models might be difficult to in-

We perform `SpECTRE` simulations with both the high- and low-stitch EoSs and NSs with central density of $\rho_c = 4.67\rho_{\rm nuc}$, above the transition density from nuclear to quark matter; see the red dots in Fig. 8. Preliminary results with low spatial resolutions demonstrated that for such $\rho_c > \rho_t$, the NS undergoes strong density oscillations that are quickly damped. Given that the fundamental mode is long-lived [96], this short damping timescale is probably related to numerical dissipation. Therefore we perform and compare simulations at various grid resolutions to ensure convergence, increasing the number of computational elements while the number of grid points inside each element is fixed.[7] The main results presented below correspond to a ~ 70 m resolution. We also restrict to the low-stitch fit since the differences between the low- and high-stitch fits are likely resolvable for < 130 m resolution, see Fig. 8.

The finite-difference solver needs to compute the solution (in our case ρ, p, and Wv^i, where W is the Lorentz factor and v^i the spatial velocity) at cell interfaces (halfway between grid points). We compute these using two different reconstruction schemes: the widely employed monotonized central [97] and a positivity-preserving adaptive order scheme which was recently implemented in `SpECTRE` [98]. In the n-th order adaptive scheme, we first try reconstructing the finite-difference interface values with a degree $n-1$ polynomial without any limiting procedure. If the reconstructed values are (i) not positive or (ii) trigger a certain oscillation-detecting criterion, we repeat the reconstruction with progressively lower-order methods. In this work we use the fifth-order adaptive scheme which first tries reconstruction with a quartic polynomial and switches to monotonized central if the reconstructed values fail to satisfy the conditions described above. Finally, if the monotonized central reconstruction did not produce positive values at the interface, first-order reconstruction is used.

We plot the central density and the spectrum in the top and bottom panels of Fig. 9 for both reconstruction schemes. We find good agreement in the frequency and damping time of the density modes, though the monotonized central scheme predicts more than double the power of the adaptive order method below ~ 80 kHz. Interestingly, we find that the presence of a quark core in the NS changes the spectrum qualitatively,

---

terpret, as a 1% interpolation inconsistency in $\rho(p)$ can lead to differences of $\mathcal{O}(100$ m$)$ on the second stable branch. This problem is more pronounced here as the DBHF_2507 construction requires computing $\rho(e) = 2.5\rho_{\rm nuc}$ via table-based root finding, a procedure that depends on the interpolation strategy and, in turn, affects the transition mass and radius. For hadronic EoSs this issue is suppressed, as differences in interpolation are smoothed over by the integration of the TOV equations. The enthalpy parametrization, having an analytic expression for $e(\rho)$, does not face this issue.

[7] We use a sixth-order (P_5) discontinuous Galerkin scheme, where each element uses 6^3 grid points on the discontinuous Galerkin mesh.
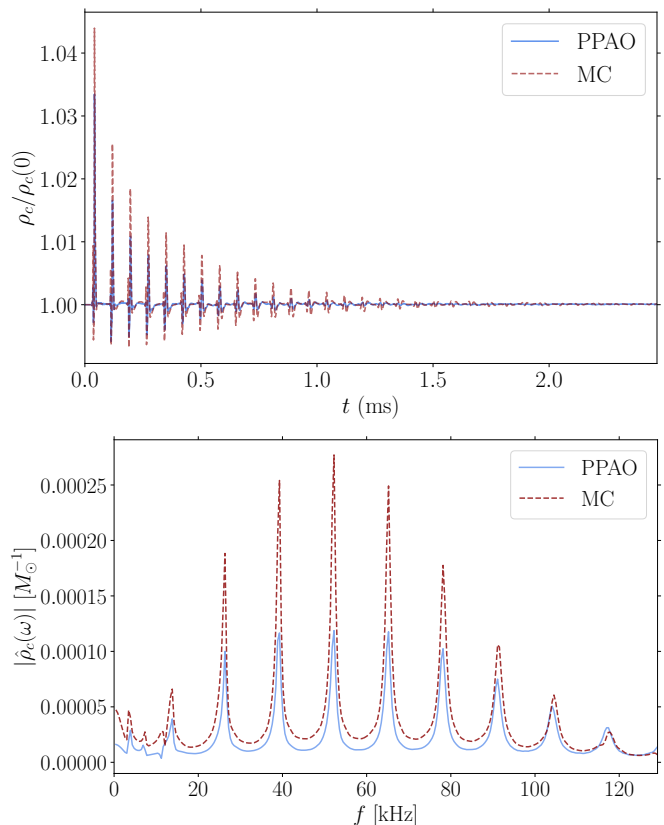

Figure 9. Normalized NS central density as a function of time (top panel) and its spectrum (bottom panel) for `SpECTRE` simulations with enthalpy fits to the DBHF_2507 nuclear EoS that are stitched to the spectral parametrization at $\rho_{\rm nuc}$ for two different choices of finite-difference reconstruction schemes. The adapative order reconstructor is marked in blue and the monotonized central reconstructor is marked in red. Run details are listed as enthalpy-pt-ppao-70 and enthalpy-pt-mc-70 respectively in Table II. The simulated star has a central density of $\sim 4.67\rho_{\rm nuc}$; it is marked in Fig. 8. We find excellent agreement on mode frequencies but slight differences in power distribution.

c.f., Fig. 7. The spectrum is now dominated by modes in the $\mathcal{O}(10)$ kHz range, an order of magnitude higher than the hadronic NS case of Fig. 7. The spacing of the modes, about 16 kHz, is of order $c/2R_{\rm core}$, where $R_{\rm core} \sim 6$ km is the radius of the quark core. We attribute this to density perturbations that are confined to the quark core and are only weakly coupled to the bulk behavior of the star across the transition. In order to confirm this, we perform a run at ~ 67 m resolution and plot the density profile of the star as a function of radius in Fig. 10 at different times. Most of the oscillation power sourced in the quark core is reflected back into the core at the quark-hadronic boundary, with only a small fraction getting transmitted into the hadronic region. The reflected pulse gets inverted (fixed-end reflection); this is consistent with theoretical expectations since the sound speed changes from $c_s^2 = 1$ in the quark core to $c_s^2 \sim 0.3$ in the

hadronic region at the boundary.

The initial perturbation needed to drive these modes is provided by numerical noise near the transition, with $\mathcal{O}(50-100\text{kHz})$ being the scale of the sound crossing frequency of a computational element of our domain. High frequency modes, in particular p-modes being primarily confined to the core of the star is in line with expectations for radial modes [99].

Simulation runtimes are provided in Table II. We find that the adaptive-order simulation (enthalpy-pt-ppao-70) has a $\sim 20\%$ longer runtime than the monotonized central (enthalpy-pt-mc-70) simulation, which is expected. Turning to the EoS and comparing enthalpy-pt-mc-130 and enthalpy-dbhf-mc-130 at identical resolutions, number of CPUs, and reconstruction schemes, we find a $\mathcal{O}(40\%)$ increase in runtime for DBHF_2507 as compared to DBHF. We do not attribute this runtime slowdown to increased EoS evaluation time, as the enthalpy EoS employed beyond the phase transition uses no trigonometric correction terms, and thus is nearly computationally identical to the polytrope profiled in Table III. This indicates that individual EoS evaluations (above the transition) are actually somewhat cheaper than in either of the fits to DBHF, discussed in Sec. V (below the transition they are identical). Instead, we attribute the slowdown to the non-smoothness of this EoS; $p(\rho)$ is not analytically $\mathcal{C}^1$ across the phase transition, and $\rho(p)$ is an incredibly sensitive function near the transition. Since our default primitive recovery scheme requires root-finding to determine $\rho(p)$ [100], this can result in significant slowdowns.

Comparing the simulations enthalpy-pt-mc-130 and enthalpy-pt-mc-70, we also find that refining the grid resolution from 134 m to 67 m results in only a 4-fold increase in runtime, compared to the expected $(134/67)^3 = 8$.[8] We attribute this lower-than-expected increase to the DG-FD hybrid scheme [50]. At higher resolutions each cell is smaller, therefore finite-difference cells are more tightly concentrated in regions with discontinuities. This results in a lower fraction of the NS reverting to the slower finite-difference scheme from the faster discontinuous Galerkin scheme. We display a slice of the NS for enthalpy-pt-ppao-70 in Fig. 11, and mark the cells which have reverted to finite-difference in red. The majority of the NS interior is indeed using the discontinuous Galerkin method, with finite difference being used only at the phase-transition and surface interfaces.

2. Smooth transitions

Due to its flexibility, the enthalpy parametrization can also be used to model smoother transitions in the EoS,

such as those that may arise from a crossover transition. To demonstrate this, we begin with DBHF_2507 and average the speed of sound at nearby points over the entire EoS. This is distinct from the small perturbation added to the EoS in in Sec. V C, as in this case we expect the resulting EoS to be well described by a smooth interpolant. To demonstrate this, we fit this new smoothed EoS with $j_{\max} = 4$ trigonometric terms and display the fit in Fig. 12. We find sub-1% agreement in the $1-2\rho_{\text{nuc}}$ density region which most directly affects macroscopic observables. Relative errors are typically higher below the enthalpy-spectral transition point (set to ρ_{nuc} here). This is because smoothing the EoS is done by locally averaging the speed of sound, so that after averaging the speed of sound is locally close to being constant. For polytropic and nearly polytropic EoSs the speed of sound is not nearly constant at low densities, so a spectral parametrization cannot effectively fit the smooth c_s^2 EoS.

We expect simulating NSs with EoSs displaying smooth but rapidly varying speeds of sound to be slower. This is for two primary reasons. First, fitting EoSs to some fixed degree of precision for more complicated EoSs typically requires adding more parameters, increasing evaluation time. Second, EoSs with rapid changes in $dp/d\rho$ tend to slow down primitive recovery, as the function $\rho(p)$ must be evaluated by root-finding. Even though the EoS in this case is analytically smooth, root-finding algorithms require more evaluations if the function is quickly varying. Overall, the EoS presented in Fig. 12 requires a comparable time per evolution step to enthalpy-dbhf-mc-130 indicating the EoS is "smooth" enough for fast evolution.

In general, we expect smooth EoSs to be most effectively represented by globally smooth parametrizations, while EoSs with discontinuities will be better modeled by piecewise parametrizations. In addition, nonsmoothness can lead to a loss of accuracy in simulations [41], so an additional trade-off may exist between accuracy and performance in the choice to use a smooth versus a piecewise interpolant. The enthalpy parameterization is flexible enough to be effective in both the piecewise EoS and the smooth EoS cases.

VI. DISCUSSION

We introduced a new enthalpy-based parametrization for the cold nuclear EoS that can capture a wide range nuclear models and their phenomenological extensions using polynomials and trigonometric terms. The *enthalpy parametrization* emphasizes *flexibility*, as it is able to effectively model both smooth and non-smooth nuclear models, and *computational performance* as its evaluation cost scales with the number of parameters used. For example, it displays comparable performance to single-polytrope parametrizations for the case of polytropic EoSs, while the computational cost scales with the num-

---

[8] We run each simulation for 40,000 CFL-limited time steps [101], so refining the grid does not lead to any major slowdown from time stepping. This would not be the case if we ran to a fixed final time.
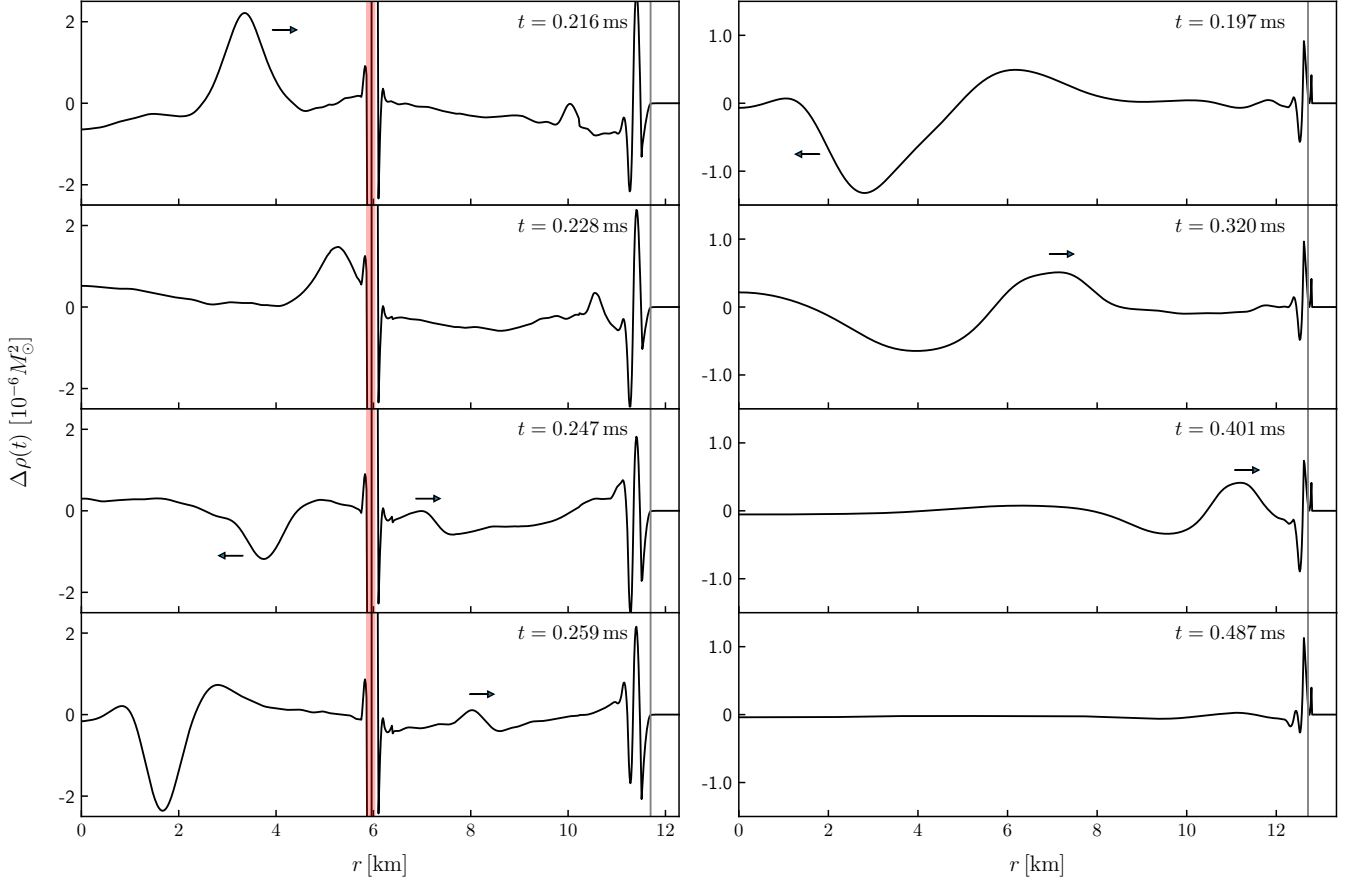
Figure 10. Rest-mass density profile relative to the initial profile $\Delta\rho \equiv \rho(r,t) - \rho(r,0)$ as a function of radius for a hybrid star described with DBHF_2507 (left panel; details in Sec. V C) and a simple polytrope with $\Gamma = 2$ (right panel; details in App. B) for different times (top to bottom). We denote the NS surface with a vertical solid gray line in each panel and the quark-hadronic boundary with a vertical red line in the left panel. We show snapshots of the density at four different times in order to examine the dynamical behavior of the density oscillations. For the hybrid star (left) density perturbations are partially transmitted and reflected at the quark-hadronic boundary, while for the polytrope (right) the wave smoothly propagates back and forth within the NS interior. Small black arrows highlight the wave packet and its traveling direction. The hybrid star snapshots are from the run enthalpy-pt-ppao-70 and the polytrope snapshots are from a simulation with identical domain, finite-difference reconstruction scheme, and central density, but a polytropic EoS (B6) in place of DBHF_2507. See polytropic-polytrope-mc-130 for details of a lower-resolution polytropic simulation.

ber of fit parameters for more complex (such as non-smooth) models. This trade-off between computational performance and flexibility, allows us to tune EoS fits to the resolution requirements of the problem at hand.

Computational performance is achieved by inexpensive evaluation of the various thermodynamic quantities. The $p(\rho)$ evaluation cost does not exceed $\mathcal{O}(4)$ times that of a polytropic EoS for any case we investigated, even when many trigonometric terms are used. In cases where this slowdown is significant, the enthalpy parametrization may be sped up significantly by using Clenshaw's method [74]. We obtain faster evaluation of $\epsilon(\rho)$ than the existing spectral parametrization in all cases, as the latter evaluates ϵ numerically, while the enthalpy parametrization computes all thermodynamic quantities analytically. Overall, the additional compu-

tational cost of the enthalpy parametrization on top of other existing parametrizations is always smaller than the cost of other simulation components.

With the caveat that quantifying EoS fitting accuracy is subtle and depends on the parameters one compares, we overall find that the enthalpy parametrization is able to successfully fit nuclear models. In principle and in the context of numerical simulations, EoS parametrizations need only fit the nuclear EoS as well as the simulation resolution. Nonetheless, even subpercent errors in the pressure near $\rho_{\mathrm{nuc}} - 2\rho_{\mathrm{nuc}}$ can lead to ~ 100 m differences in NS radii. In contrast to lower-dimensional or less flexible parametrizations, we show that the enthalpy parametrization is able to fit tabulated and phenomenological nuclear models to effectively arbitrary precision by using additional parameters. The optimal number of
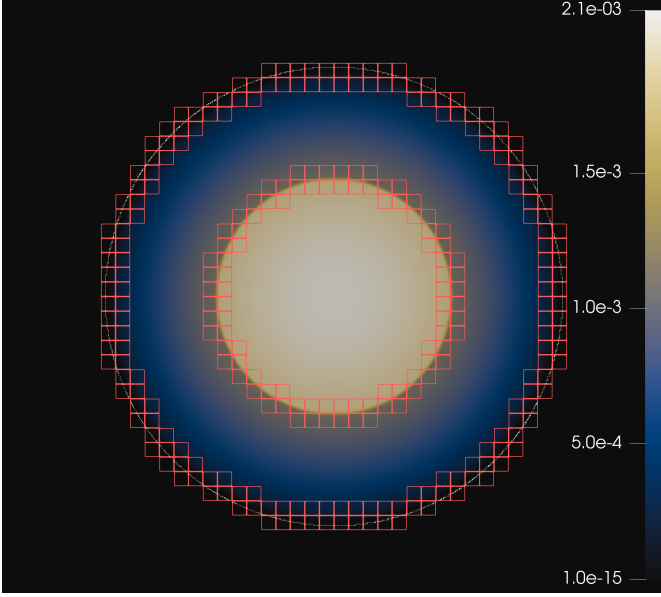
Figure 11. NS rest mass density (colorbar, units of $M_\odot^{-2}$) on the $y-z$ plane at $t = 100 M_\odot$ for the run enthalpy-pt-ppao-70. Red marks subdomain elements where finite-difference is used. The finite-difference cells are confined near the NS surface (outer circle, white solid line) and the phase transition layer (inner circle) where discontinuities are expected. The majority of the star is still evolved with the more computationally efficient discontinuous-Galerkin method.
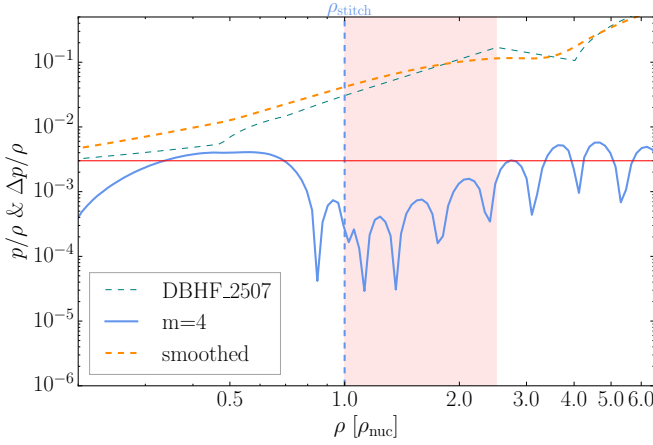

Figure 12. Same as Fig. 5 but for the smoothed version of DBHF_2507 constructed in Sec. V C 2. The enthalpy parametrization achieves sub-1% errors in the most relevant region, $1 - 2\rho_{\rm nuc}$.

parameters is then determined by balancing accuracy and computational cost for a given numerical resolution.

The enthalpy parametrization's flexibility allows us to efficiently and with little fine tuning represent both smooth and non-smooth nuclear models. The latter may correspond to models with strong phase transitions that we can fit and numerically evolve using SpECTRE. Our simulations demonstrate that we can stably evolve such

stars in the Cowling approximation. However, studying the evolution of hybrid hadronic-quark NSs away from an unstable EoS branch that falls between the hadronic and the quark branches [102] hinges on full metric evolution coupled to GRMHD. SpECTRE's hybrid DG-FD scheme is crucial for the computational performance of these simulations. The DG-FD scheme allows phase transitions to be modeled with lower-order finite-difference methods while continuing to use higher-order discontinuous-Galerkin methods throughout the individual hadronic and quark regions. This leads to better computational scaling than might be expected upon mesh refinement, as better resolution of boundaries (such as the quark-hadronic matter boundary) within the star reduces the amount of the domain which uses the slower finite-difference approach.

The enthalpy parametrization is a step toward ensuring that numerical simulations can efficiently represent a wide range of nuclear phenomenology. Accurate simulations of NSs will continue being crucial for the interpretation of new astrophysical and experimental data. Even with current EoS constraints, the space of potential BNS phenomenology is large, and many questions remain regarding the impact of magnetic fields, instabilities, temperature effects [103, 104] and transport physics. Future steps include extending the applicability of the enthalpy parametrization beyond cold, beta-equilibrated nuclear matter, and incorporating more physical effects in SpECTRE simulations.

The simulations presented here were performed with SpECTRE commit hash 2df19579a84385b3d5ab4663e3da7e33012e0355. The earliest release of SpECTRE with this commit is version 2023.01.13 [105]. Input files for the runs performed, including enthalpy fit parameters for each EoS studied, are available on Github [106].
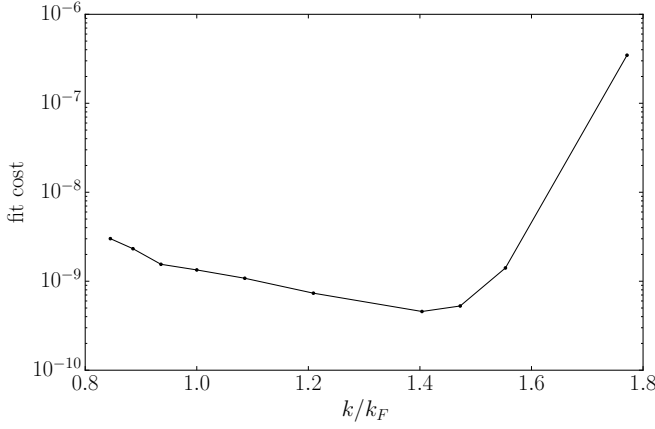
Figure 13. Cost, Eq A1, in arbitrary units, of the fit to the phenomenological EoS of Fig. 1 as a function of k. The minimum occurs at k slightly larger than k_F, in this case near $k = 1.4k_F$.

Appendix A: Fitting the enthalpy parametrization

In this Appendix we provide details about the procedure with which we fit some tabulated EoS data with the enthalpy parametrization which includes the following parameters:

- The upper ρ_{max} and lower ρ_{min} density limits are chosen based on the densities of interest. For NS simulations, reasonable values are $\rho_{min} = \rho_{nuc}$, $\rho_{max} = 7\rho_{nuc}$, but the upper limit depends on the maximum density expected in the simulation.

- The scaling parameters ρ_0 and the wavenumber of the trigonometric correction terms k are not fit, but rather fixed. When we extend a model via a constant speed of sound, Sec. V C, the choice of ρ_0 is determined by the modeling problem. When the EoS is fit, ρ_0 is chosen $\rho_0 \in (0, \rho_{min}]$, so that $z_{max} = \log(\rho_{max}/\rho_0) \lesssim i_{max}$, see Sec. C. We find $\rho_0 = \rho_{min}/2$ is generally a robust choice. Analogous to how ρ_0 controls the scale of polynomial terms, k controls the scale of trigonometric oscillations. As described in Sec. III, typically $k \approx k_F$ is a good choice, but small perturbations $k \in [k_F/2, 2k_F]$ may improve the fit quality for certain problems, depending on the details of the EoS. Figure 13 shows that the effect of varying k is small for the particular test problem displayed in Fig. 1.

- The parameters i_{max} and j_{max} determine the number of polynomials and trigonometric terms respectively; see Eq. (9) and Eq. (10). The quality of the fit is a strong function of i_{max} and j_{max}, but increasing j_{max} above ~ 10 comes at a considerable computational cost even at low resolutions. On the other hand the cost of increasing i_{max} is small, typically of order 2% or less of the total cost of the $p(\rho)$ evaluation per additional polynomial term.

- The coefficients of the polynomial γ_i, Eq. (9), and the trigonometric a_j, b_j, Eq. (10), expansion are fit through a linear least-squares approach.

Given a target EoS with enthalpy $h(z_i)$ at discrete densities z_i, the linear fit is based on minimizing the cost function

$$C(a_j, b_j, c_i) = \sum_k \left(\frac{h_*(z_k; a_j, b_j, c_i) - h(z_k)}{\sigma(z)} \right)^2 , \quad (A1)$$

where h_* is given in Eq. (12). The factor $\sigma(z)$ is the fit tolerance which can be chosen such that the fit is optimal at different density regions. We choose to target similar relative uncertainty on the non-rest-mass component of the enthalpy density $(h-1)\rho = p+e$ across density scales: $\sigma(z) \propto \rho(z) \propto \exp(z)$. Overall, the tolerance scales as $1/\rho$, so the fit is relatively better (with respect to h) at low densities.

Finally, the EoS fit is completed by stitching to some other EoS parametrizaton at $\rho_{stitch} = \rho_{min}$. In the majority of cases this is the spectral parametrization, though we also explore another enthalpy segment in Sec. V C and a polytrope in App. B. The low-density spectral EoS itself transitions to a lower-density polytrope at some fixed reference density ρ_r. Following Ref. [41], we define $x \equiv \log(\rho/\rho_r)$ and write the spectral pressure as

$$p_s(x) = \begin{cases} p_0 \exp[\Gamma_0 x] & x \leq 0, \\ p_0 \exp\left[\sum_{i=0}^3 \frac{1}{i+1}\Gamma_i x^{i+1}\right] & x > 0, \end{cases} \quad (A2)$$

where p_0 controls the overall pressure, and Γ_0, Γ_i are the spectral coefficients. The low-density behavior fixes Γ_0, while requiring a $\mathcal{C}^1$ transition to the enthalpy parametrization, i.e., continuity in pressure, energy density, and pressure derivative fixes 3 more parameters.

The remaining 1 degree of freedom is selected by either maximizing smoothness across the lower-density transition to the polytrope or maximizing accuracy of the low-density EoS. Smoothness is prioritized when the stitching density is below the core density of typical NS. Then, we set $\Gamma_1 = 0.0$ [41], guaranteeing that Eq. (A2) is $\mathcal{C}^2$ across the transition ρ_r. This typically produces good fits to the overall $M-R$ curve for the entire EoS. If the spectral parametrization is stitched to the enthalpy parametrization at a higher density (near the core density of astrophysical NSs as is the case in the high-stitch fit of Sec.V) we instead allow Γ_1 to vary, choosing it to maximize the agreement of the total parametrized EoS with

the target. Both strategies typically result in accurate $\mathcal{C}^1$-stitching to the enthalpy parametrization, with residuals much smaller than mismodeling in the low-density regime.

Appendix B: Approximating a single polytrope

As an example of the strategy for fitting a target EoS with the enthalpy parametrization, we consider a single-polytrope. In this case, the enthalpy coefficients can be computed analytically. The general goal is to express the EoS in the form of Eq. (8), i.e., compute the enthalpy as a function of log-density.

The polytropic exponent is defined as

$$\Gamma(z) \equiv \frac{d \log p}{d \log \rho} = \frac{\rho}{p} \frac{dh}{dz} = \frac{\rho}{p} \frac{d \left(\frac{1}{\rho} \frac{de}{dz} \right)}{dz} \,. \qquad (B1)$$

For a constant polytropic exponent $\Gamma(z) = \Gamma_0$ and using the identity

$$p(z) = h(z)\rho(z) - e(z) = \frac{de}{dz} - e(z) \,, \qquad (B2)$$

Eq. (B1) becomes

$$\frac{d^2 e}{dz^2} - (\Gamma_0 + 1)\frac{de}{dz} + \Gamma_0 e = 0 \,. \qquad (B3)$$

The solution to this differential equation is

$$e(z) = (e_0 - \rho_0)\exp(\Gamma_0 z) + \rho_0 \exp(z) \,, \qquad (B4)$$

where we have enforced $e(z = 0) = e_0$ and $e(z \to -\infty) \to \rho(z)$[9] and the enthalpy is

$$h(z) = \frac{1}{\rho}\frac{de}{dz} = \frac{e_0 - \rho_0}{\rho_0}\Gamma_0 \exp\left[(\Gamma_0 - 1)z\right] + 1 \,. \qquad (B5)$$

Comparing with Eq. (9) the polynomial coefficients of the enthalpy expansion are $\gamma_i = h_0 (\Gamma_0 - 1)^i / i!$, with $h_0 = \Gamma_0 (e_0 - \rho_0) / \rho_0$, if $i \neq 0$, and $\gamma_0 = h_0 (\Gamma_0 - 1) + 1$. In practice, evaluating the polynomial expansion of Eq. (9) requires many floating point operations. Nonetheless, this computation is not necessarily slower than evaluating a simple polytrope if Γ_0 is not an integer, because floating-point exponentiation typically at least an order of magnitude slower than multiplication and addition.

We use this enthalpy parametrization of the polytrope model to compare against the direct single-polytrope SpECTRE implementation and verify the predicted Cowling-approximation NS modes [51, 111]. The

---

[9] This is equivalent to assuming the specific internal energy ϵ is 0 in ordinary, low-density cold matter. This can be done by defining the baryon "rest" mass to be the average mass of a baryon in the outer crust of a NS (despite the fact these baryons may be bound in, e.g. iron and therefore differ from the mass of a free neutron/proton by up to 1%).
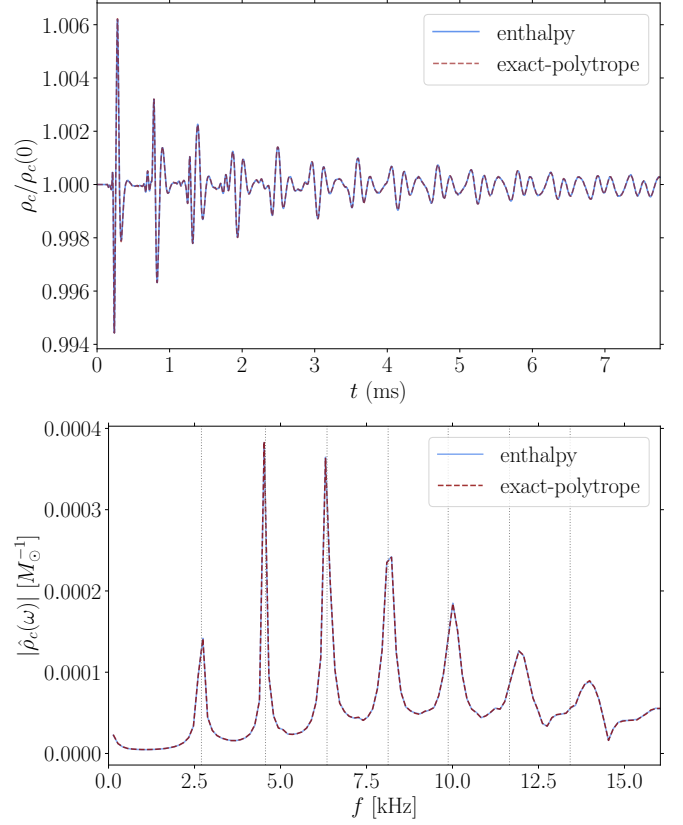

Figure 14. NS central density as a function of time (top panel) and its spectrum (bottom panel) for SpECTRE simulations with an enthalpy fit to a single polytrope with $\Gamma_0 = 2.0$ (blue) and a direct single-polytropic parametrization (red, dashed,). Known Cowling frequencies [111] are marked as dashed vertical lines. The spectra are identical by eye.

low-density EoS in the enthalpy parametrization case is stitched to the exact polytropic expression

$$P(\rho) = \frac{100}{M_\odot^{-2.0}}\rho^{2.0} \,. \qquad (B6)$$

We evolve a NS with central density $1.28 \times 10^{-3} M_\odot^{-2} \approx 2.84\rho_{\rm nuc}$, which is the same as the stars evolved in Refs. [51, 111]. The number of terms necessary in the polynomial expansion depends on the desired accuracy. For a resolution of 130 m we find that $i_{\rm max} = 8$ is more than sufficient. This is consistent with theoretical expectations, as the first neglected term, is of order $1/9! \approx 2 \times 10^{-6}$, indicating errors should be of this scale or smaller. Results are shown in Fig. 14 where the enthalpy fit to the polytrope and the direct single-polytropic parametrization return essentially identical results. We display the run details in Table II, as enthalpy-polytrope-mc-130 and polytropic-polytrope-mc-130.

We find effectively no difference in the runtime for the simulations using each of the polytropic and enthalpy parametrizations. Examining the cost of individual EoS calls in Table III, we find the enthalpy parametrization

Evaluation Cost (ns) Parametrization	$p(\rho)$	$\epsilon(\rho)$
enthalpy	43	44
polytrope	57	58

Table III. Performance (in nanoseconds) of the enthalpy and single-polytropic fits to a single polytrope in evaluating the pressure and internal energy at $\rho = 5.0 \times 10^{-4} M_\odot^2$. The enthalpy parametrization outperforms then polytrope in both cases.

is somewhat faster in both $p(\rho)$ and $\epsilon(\rho)$ evaluation, indicating that in this case, EoS evaluation time is not a significant contribution to runtime.

The reason the polytropic EoS evaluation is not faster despite having a very simple analytic expression is the inefficiency of floating-point exponentiation. In the case of our test problem the floating point exponent 2.0 is only known during runtime, and so the compiler cannot optimize EoS calls. If the exponent is known to be an integer at compile time, the calls can be evaluated using repeated multiplication. We implement this improvement for this particular test problem, and find the cost of polytropic $p(\rho)$ evaluations to be 10 ns on identical hardware, indicating a 5-fold improvement. Nonetheless, this speedup is not reflected in the total evolution runtime for resolutions of at least ~ 120 m as the EoS evaluation cost is subdominant to other simulation components.

Appendix C: Numerical considerations for enthalpy coefficients

Here we expand upon numerical considerations for choices of polynomial, coefficients γ_i. The choice, $\gamma_i \geq 0$ in Eq. (9) effectively bounds the number of terms in the polynomial expansion which can be practically used. To see this, consider $z_{max} \equiv \log(\rho_{max}/\rho_0)$. Coefficients γ_i must satisfy $\gamma_i z_{max}^i \lesssim \mathcal{O}(\gamma_0) \sim 1$, otherwise they would be larger than the total enthalpy in this region, which is typically also of this scale. With this in mind, we consider i as "too large" if $i \gg z_{max}$, as any term which satisfies $\gamma_i z_{max}^i \lesssim \gamma_0$ has

$$\frac{\gamma_i z^i}{\gamma_i z_{max}^i} = \left(\frac{z}{z_{max}}\right)^i, \tag{C1}$$

small except when z is nearly z_{max}. That is, the degree of freedom is only relevant at the highest densities, and this density region shrinks as i gets larger. For typical scales, such as $\rho_0 = 0.5\rho_{nuc}$, $\rho_{min} = \rho_{nuc}$, and $\rho_{max} = 7\rho_{nuc}$, then $z_{max} \sim \log(14) \approx 2.6$.

One can decrease ρ_0 to increase the relevant value of z_{max}, but this requires adding more parameters, which may not be desirable, since many of them may be irrelevant, or degenerate. One way to view this, is that in the Taylor expansion of the exponential function (equivalently the expansion of $h(z)$ in a constant speed of sound

case), the term $z^i/i!$ is the largest term on $z \in (i-1, i)$, and is generally decreasing in relevance away from this region relative to other terms. Therefore the ith term of this expansion is most relevant near $z \lesssim i$, and is unimportant far from this region. This implies that flexibility is essentially equidistributed in $\log(\rho)$ for this approximation (the same argument applies to the spectral parametrization), and that higher polynomial terms cannot resolve features at low densities. Instead, we choose to switch to a new function basis at this point, optimized to capture the largest scale features at lowest order of approximation.

[1] B. P. Abbott *et al.* (LIGO Scientific Collaboration, Virgo Collaboration), Phys. Rev. Lett. **119**, 161101 (2017), arXiv:1710.05832 [gr-qc].

[2] B. P. Abbott *et al.* (LIGO Scientific, Virgo, Fermi GBM, INTEGRAL, IceCube, AstroSat Cadmium Zinc Telluride Imager Team, IPN, Insight-Hxmt, ANTARES, Swift, AGILE Team, 1M2H Team, Dark Energy Camera GW-EM, DES, DLT40, GRAWITA, Fermi-LAT, ATCA, ASKAP, Las Cumbres Observatory Group, OzGrav, DWF (Deeper Wider Faster Program), AST3, CAASTRO, VINROUGE, MAS-TER, J-GEM, GROWTH, JAGWAR, CaltechNRAO, TTU-NRAO, NuSTAR, Pan-STARRS, MAXI Team, TZAC Consortium, KU, Nordic Optical Telescope, ePESSTO, GROND, Texas Tech University, SALT Group, TOROS, BOOTES, MWA, CALET, IKI-GW Follow-up, H.E.S.S., LOFAR, LWA, HAWC, Pierre Auger, ALMA, Euro VLBI Team, Pi of Sky, Chandra Team at McGill University, DFN, ATLAS Telescopes, High Time Resolution Universe Survey, RIMAS, RATIR, SKA South Africa/MeerKAT), Astrophys. J. Lett. **848**, L12 (2017), arXiv:1710.05833 [astro-ph.HE].

[3] T. Dietrich, T. Hinderer, and A. Samajdar, Gen. Rel. Grav. **53**, 27 (2021), arXiv:2004.02527 [gr-qc].

[4] K. Chatziioannou, Gen. Rel. Grav. **52**, 109 (2020), arXiv:2006.03168 [gr-qc].

[5] J. Piekarewicz, (2022), arXiv:2209.14877 [nucl-th].

[6] B. P. Abbott *et al.* (LIGO Scientific, Virgo), Astrophys. J. Lett. **892**, L3 (2020), arXiv:2001.01761 [astro-ph.HE].

[7] H. T. Cromartie *et al.*, Nature Astron. **4**, 72 (2019), arXiv:1904.06759.

[8] E. Fonseca *et al.*, Astrophys. J. Lett. **915**, L12 (2021), arXiv:2104.00880 [astro-ph.HE].

[9] M. C. Miller, C. Chirenti, and F. K. Lamb, (2019), arXiv:1904.08907 [astro-ph.HE].

[10] M. C. Miller *et al.*, Astrophys. J. Lett. **918**, L28 (2021), arXiv:2105.06979 [astro-ph.HE].

[11] T. E. Riley *et al.*, Astrophys. J. Lett. **887**, L21 (2019), arXiv:1912.05702 [astro-ph.HE].

[12] T. E. Riley *et al.*, Astrophys. J. Lett. **918**, L27 (2021), arXiv:2105.06980 [astro-ph.HE].

[13] J. Antoniadis, P. C. Freire, N. Wex, T. M. Tauris, R. S. Lynch, *et al.*, Science **340**, 1233232 (2013), arXiv:1304.6875 [astro-ph.HE].

[14] D. Adhikari *et al.* (PREX), Phys. Rev. Lett. **126**, 172502 (2021), arXiv:2102.10767 [nucl-ex].

[15] D. Adhikari *et al.* (CREX), (2022), arXiv:2205.11593 [nucl-ex].

[16] B. P. Abbott *et al.* (LIGO Scientific Collaboration, Virgo Collaboration), Phys. Rev. Lett. **121**, 161101 (2018), arXiv:1805.11581 [gr-qc].

[17] R. Essick, (2021), arXiv:2111.04244 [astro-ph.HE].

[18] P. T. H. Pang, I. Tews, M. W. Coughlin, M. Bulla, C. Van Den Broeck, and T. Dietrich, Astrophys. J. **922**, 14 (2021), arXiv:2105.08688 [astro-ph.HE].

[19] G. Raaijmakers *et al.*, Astrophys. J. Lett. **893**, L21 (2020), arXiv:1912.11031 [astro-ph.HE].

[20] G. Raaijmakers, S. K. Greif, K. Hebeler, T. Hinderer, S. Nissanke, A. Schwenk, T. E. Riley, A. L. Watts, J. M. Lattimer, and W. C. G. Ho, (2021), arXiv:2105.06981 [astro-ph.HE].

[21] P. Landry, R. Essick, and K. Chatziioannou, Phys. Rev. D **101**, 123007 (2020), arXiv:2003.04880 [astro-ph.HE].

[22] I. Legred, K. Chatziioannou, R. Essick, S. Han, and P. Landry, Phys. Rev. D **104**, 063003 (2021).

[23] C. Drischler, A. Carbone, K. Hebeler, and A. Schwenk, Phys. Rev. C **94**, 054307 (2016), arXiv:1608.05615 [nucl-th].

[24] L. Antón, O. Zanotti, J. A. Miralles, J. M. Martí, J. M. Ibáñez, J. A. Font, and J. A. Pons, The Astrophysical Journal **637**, 296 (2006).

[25] J. A. Font, Living Rev. Rel. **11**, 7 (2008).

[26] T. W. Baumgarte and S. L. Shapiro, *Numerical Relativity: Solving Einstein's Equations on the Computer* (Cambridge University Press, 2010).

[27] L. Baiotti and L. Rezzolla, Rept. Prog. Phys. **80**, 096901 (2017), arXiv:1607.03540 [gr-qc].

[28] D. Radice, S. Bernuzzi, and A. Perego, Ann. Rev. Nucl. Part. Sci. **70**, 95 (2020), arXiv:2002.03863 [astro-ph.HE].

[29] F. Foucart, Front. Astron. Space Sci. **7**, 46 (2020), arXiv:2006.10570 [astro-ph.HE].

[30] K. Kyutoku, M. Shibata, and K. Taniguchi, Living Rev. Rel. **24**, 5 (2021), arXiv:2110.06218 [astro-ph.HE].

[31] L. Rezzolla and O. Zanotti, *Relativistic Hydrodynamics* (Oxford University Press, 2013).

[32] B. Margalit and B. D. Metzger, Astrophys. J. **850**, L19 (2017), arXiv:1710.05938 [astro-ph.HE].

[33] D. Radice and L. Dai, Eur. Phys. J. A **55**, 50 (2019), arXiv:1810.12917 [astro-ph.HE].

[34] M. Shibata, E. Zhou, K. Kiuchi, and S. Fujibayashi, Phys. Rev. D **100**, 023015 (2019), arXiv:1905.03656 [astro-ph.HE].

[35] S. Köppel, L. Bovard, and L. Rezzolla, Astrophys. J. Lett. **872**, L16 (2019), arXiv:1901.09977 [gr-qc].

[36] E. Annala, T. Gorda, E. Katerini, A. Kurkela, J. Nättilä, V. Paschalidis, and A. Vuorinen, Phys. Rev. X **12**, 011058 (2022), arXiv:2105.05132 [astro-ph.HE].

[37] A. Camilletti, L. Chiesa, G. Ricigliano, A. Perego, L. C. Lippold, S. Padamata, S. Bernuzzi, D. Radice, D. Logoteta, and F. M. Guercilena, (2022), 10.1093/mnras/stac2333, arXiv:2204.05336 [astro-ph.HE].

[38] S. Typel *et al.*, (2022), arXiv:2203.03209 [astro-ph.HE].

[39] D. M. Siegel, P. Mösta, D. Desai, and S. Wu, Astrophys. J. **859**, 71 (2018), arXiv:1712.07538 [astro-ph.HE].

[40] J. S. Read, B. D. Lackey, B. J. Owen, and J. L. Friedman, Phys. Rev. D **79**, 124032 (2009), arXiv:0812.2163 [astro-ph].

[41] F. Foucart, M. D. Duez, A. Gudinas, F. Hebert, L. E. Kidder, H. P. Pfeiffer, and M. A. Scheel, Phys. Rev. D **100**, 104048 (2019), arXiv:1908.05277 [gr-qc].

[42] C. A. Raithel and V. Paschalidis, Phys. Rev. D **106**, 023015 (2022), arXiv:2204.00698 [gr-qc].

[43] L. Lindblom, Phys. Rev. D **82**, 103011 (2010), arXiv:1009.0738 [astro-ph.HE].

[44] S. K. Greif, G. Raaijmakers, K. Hebeler, A. Schwenk, and A. L. Watts, Mon. Not. Roy. Astron. Soc. **485**, 5363 (2019), arXiv:1812.08188 [astro-ph.HE].

[45] L. Lindblom, Astrophys. J. **398**, 569 (1992).

[46] N. Deppe, W. Throwe, L. E. Kidder, N. L. Vu, F. Hébert, J. Moxon, C. Armaza, G. S. Bonilla, Y. Kim, P. Kumar, G. Lovelace, A. Macedo, K. C. Nelli,

E. O'Shea, H. P. Pfeiffer, M. A. Scheel, S. A. Teukolsky, N. A. Wittek, *et al.*, "SpECTRE v2022.08.01," 10.5281/zenodo.6949324 (2022).

[47] L. E. Kidder *et al.*, J. Comput. Phys. **335**, 84 (2017), arXiv:1609.00098 [astro-ph.HE].

[48] L. Kale, B. Acun, S. Bak, A. Becker, M. Bhandarkar, N. Bhat, A. Bhatele, E. Bohm, C. Bordage, R. Brunner, R. Buch, S. Chakravorty, K. Chandrasekar, J. Choi, M. Denardo, J. DeSouza, M. Diener, H. Dokania, I. Dooley, W. Fenton, J. Galvez, F. Gioachin, A. Gupta, G. Gupta, M. Gupta, A. Gursoy, V. Harsh, F. Hu, C. Huang, N. Jagathesan, N. Jain, P. Jetley, P. Jindal, R. Kanakagiri, G. Koenig, S. Krishnan, S. Kumar, D. Kunzman, M. Lang, A. Langer, O. Lawlor, C. W. Lee, J. Lifflander, K. Mahesh, C. Mendes, H. Menon, C. Mei, E. Meneses, E. Mikida, P. Miller, R. Mokos, V. Narayanan, X. Ni, K. Nomura, S. Paranjpye, P. Ramachandran, B. Ramkumar, E. Ramos, M. Robson, N. Saboo, V. Saletore, O. Sarood, K. Senthil, N. Shah, W. Shu, A. B. Sinha, Y. Sun, Z. Sura, E. Totoni, K. Varadarajan, R. Venkataraman, J. Wang, L. Wesolowski, S. White, T. Wilmarth, J. Wright, J. Yelon, and G. Zheng, "Uiuc-ppl/charm: Charm++ version 6.10.2," (2020).

[49] T. G. Cowling, mnras **101**, 367 (1941).

[50] N. Deppe, F. Hébert, L. E. Kidder, and S. A. Teukolsky, Classical and Quantum Gravity **39**, 195001 (2022).

[51] N. Deppe *et al.*, Phys. Rev. D **105**, 123031 (2022), arXiv:2109.12033 [gr-qc].

[52] L. Lindblom and N. M. Indik, Phys. Rev. **D89**, 064003 (2014), [Erratum: Phys. Rev.D93,no.12,129903(2016)], arXiv:1310.0803 [astro-ph.HE].

[53] S. Han and A. W. Steiner, Phys. Rev. D **99**, 083014 (2019), arXiv:1810.10967 [nucl-th].

[54] P. T. H. Pang, T. Dietrich, I. Tews, and C. Van Den Broeck, Phys. Rev. Res. **2**, 033514 (2020), arXiv:2006.14936 [astro-ph.HE].

[55] D. Wysocki, R. O'Shaughnessy, L. Wade, and J. Lange, (2020), arXiv:2001.01747 [gr-qc].

[56] J. Blackman, S. E. Field, C. R. Galley, B. Szilágyi, M. A. Scheel, M. Tiglio, and D. A. Hemberger, Phys. Rev. Lett. **115**, 121102 (2015), arXiv:1502.07758 [gr-qc].

[57] V. Varma, S. E. Field, M. A. Scheel, J. Blackman, L. E. Kidder, and H. P. Pfeiffer, Phys. Rev. D **99**, 064045 (2019), arXiv:1812.07865 [gr-qc].

[58] M. Wijngaarden, K. Chatziioannou, A. Bauswein, J. A. Clark, and N. J. Cornish, Phys. Rev. D **105**, 104019 (2022), arXiv:2202.09382 [gr-qc].

[59] M. Breschi, S. Bernuzzi, K. Chakravarti, A. Camilletti, A. Prakash, and A. Perego, (2022), arXiv:2205.09112 [gr-qc].

[60] M. Shibata and K. Uryu, Phys. Rev. D **61**, 064001 (2000), arXiv:gr-qc/9911058.

[61] Z. B. Etienne, J. A. Faber, Y. T. Liu, S. L. Shapiro, K. Taniguchi, and T. W. Baumgarte, Phys. Rev. D **77**, 084002 (2008), arXiv:0712.2460 [astro-ph].

[62] L. Baiotti, B. Giacomazzo, and L. Rezzolla, Phys. Rev. D **78**, 084033 (2008), arXiv:0804.0594 [gr-qc].

[63] M. D. Duez, F. Foucart, L. E. Kidder, H. P. Pfeiffer, M. A. Scheel, and S. A. Teukolsky, Phys. Rev. D **78**, 104015 (2008), arXiv:0809.0002 [gr-qc].

[64] D. Radice, L. Rezzolla, and F. Galeazzi, Mon. Not. Roy. Astron. Soc. **437**, L46 (2014), arXiv:1306.6052 [gr-qc].

[65] J. DeBuhr, B. Zhang, M. Anderson, D. Neilsen, E. W.

[66] Hirschmann, T. Grenga, and S. Paolucci, Astrophys. J. **867**, 112 (2018), arXiv:1512.00386 [astro-ph.IM].

[66] K. Yagi and N. Yunes, Phys. Rev. D **88**, 023009 (2013), arXiv:1303.1528 [gr-qc].

[67] J. S. Read, C. Markakis, M. Shibata, K. Uryu, J. D. Creighton, *et al.*, Phys. Rev. D **79**, 124033 (2009), arXiv:0901.3258 [gr-qc].

[68] M. Ujevic, H. Gieg, F. Schianchi, S. V. Chaurasia, I. Tews, and T. Dietrich, (2022), arXiv:2211.04662 [gr-qc].

[69] K. Hotokezaka, K. Kyutoku, H. Okawa, M. Shibata, and K. Kiuchi, Phys. Rev. D **83**, 124008 (2011), arXiv:1105.4370 [astro-ph.HE].

[70] B. D. Lackey, K. Kyutoku, M. Shibata, P. R. Brady, and J. L. Friedman, Phys. Rev. D **89**, 043009 (2014), arXiv:1303.6298 [gr-qc].

[71] T. Dietrich, S. Bernuzzi, B. Bruegmann, and W. Tichy, in *26th Euromicro International Conference on Parallel, Distributed and Network-based Processing* (2018) pp. 682–689, arXiv:1803.07965 [gr-qc].

[72] T. Dietrich, S. Bernuzzi, and W. Tichy, Phys. Rev. **D96**, 121501 (2017), arXiv:1706.02969 [gr-qc].

[73] M. F. O'Boyle, C. Markakis, N. Stergioulas, and J. S. Read, Phys. Rev. D **102**, 083027 (2020), arXiv:2008.03342 [astro-ph.HE].

[74] W. H. Press, S. A. Teukolsky, W. T. Vetterling, and B. P. Flannery, *Numerical Recipes 3rd Edition: The Art of Scientific Computing*, 3rd ed. (Cambridge University Press, USA, 2007).

[75] J. I. Kapusta and T. Welle, Phys. Rev. C **104**, L012801 (2021), arXiv:2103.16633 [nucl-th].

[76] P. Landry and B. Kumar, Astrophys. J. **868**, L22 (2018), arXiv:1807.04727 [gr-qc].

[77] R. Essick, P. Landry, and D. E. Holz, Phys. Rev. D **101**, 063007 (2020), arXiv:1910.09740 [astro-ph.HE].

[78] P. Mösta, B. C. Mundim, J. A. Faber, R. Haas, S. C. Noble, T. Bode, F. Löffler, C. D. Ott, C. Reisswig, and E. Schnetter, Class. Quant. Grav. **31**, 015005 (2014), arXiv:1304.5544 [gr-qc].

[79] I. Tews, Frontiers in Physics **8** (2020), 10.3389/fphy.2020.00153.

[80] C. Drischler, A. Carbone, K. Hebeler, and A. Schwenk, Phys. Rev. C **94**, 054307 (2016), arXiv:1608.05615 [nucl-th].

[81] R. Essick, I. Tews, P. Landry, S. Reddy, and D. E. Holz, Phys. Rev. C **102**, 055803 (2020), arXiv:2004.07744 [astro-ph.HE].

[82] X. Roca-Maza, X. Viñas, M. Centelles, B. K. Agrawal, G. Colo', N. Paar, J. Piekarewicz, and D. Vretenar, Phys. Rev. C **92**, 064304 (2015), arXiv:1510.01874 [nucl-th].

[83] R. Essick, P. Landry, A. Schwenk, and I. Tews, Phys. Rev. C **104**, 065804 (2021).

[84] R. Essick, I. Tews, P. Landry, and A. Schwenk, Phys. Rev. Lett. **127**, 192701 (2021), arXiv:2102.10074 [nucl-th].

[85] I. Tews, J. Margueron, and S. Reddy, Phys. Rev. C **98**, 045804 (2018), arXiv:1804.02783 [nucl-th].

[86] I. Legred, K. Chatziioannou, R. Essick, and P. Landry, Phys. Rev. D **105**, 043016 (2022), arXiv:2201.06791 [astro-ph.HE].

[87] F. Douchin and P. Haensel, Astron. Astrophys. **380**, 151 (2001), arXiv:astro-ph/0111092.

[88] J. Oppenheimer and G. Volkoff, Phys. Rev. **55**, 374

(1939).

[89] T. Gross-Boelting, C. Fuchs, and A. Faessler, Nucl. Phys. A **648**, 105 (1999), arXiv:nucl-th/9810071.

[90] M. G. Alford, G. F. Burgio, S. Han, G. Taranto, and D. Zappalà, Phys. Rev. D **92**, 083002 (2015), arXiv:1501.07902 [nucl-th].

[91] J. M. Lattimer and M. Prakash, Astrophys. J. **550**, 426 (2001), arXiv:astro-ph/0002232.

[92] K. Chatziioannou and S. Han, Phys. Rev. D **101**, 044019 (2020), arXiv:1911.07091 [gr-qc].

[93] H. Gieg, T. Dietrich, and M. Ujevic, Particles **2**, 365 (2019), arXiv:1908.03135 [gr-qc].

[94] A. Kurkela, P. Romatschke, and A. Vuorinen, Phys. Rev. D **81**, 105021 (2010), arXiv:0912.1856 [hep-ph].

[95] I. Tews, J. Carlson, S. Gandolfi, and S. Reddy, Astrophys. J. **860**, 149 (2018), arXiv:1801.01923 [nucl-th].

[96] K. D. Kokkotas and J. Ruoff, Astron. Astrophys. **366**, 565 (2001), arXiv:gr-qc/0011093.

[97] B. Van Leer, Journal of Computational Physics **23**, 276 (1977).

[98] N. Deppe *et al.*, (in preparation).

[99] S. Sen, S. Kumar, A. Kunjipurayi, P. Routaray, T. Zhao, and B. Kumar, (2022), arXiv:2205.02076 [nucl-th].

[100] W. Kastaun, J. V. Kalinani, and R. Ciolfi, Phys. Rev. D **103**, 023018 (2021), arXiv:2005.01821 [gr-qc].

[101] R. Courant, K. Friedrichs, and H. Lewy, IBM Journal of Research and Development **11**, 215 (1967).

[102] P. L. Espino and V. Paschalidis, Phys. Rev. D **105**, 043014 (2022), arXiv:2105.05269 [astro-ph.HE].

[103] A. Carbone and A. Schwenk, Phys. Rev. C **100**, 025805 (2019), arXiv:1904.00924 [nucl-th].

[104] C. A. Raithel, F. Ozel, and D. Psaltis, Astrophys. J. **875**, 12 (2019), arXiv:1902.10735 [astro-ph.HE].

[105] N. Deppe, W. Throwe, L. E. Kidder, N. L. Vu, F. Hébert, J. Moxon, C. Armaza, G. S. Bonilla, Y. Kim, P. Kumar, G. Lovelace, A. Macedo, K. C. Nelli, E. O'Shea, H. P. Pfeiffer, M. A. Scheel, S. A. Teukolsky, N. A. Wittek, I. Anantpurkar, M. Boyle, A. Carpenter, A. Ceja, H. Chaudhary, F. Foucart, N. Ghadiri, M. Giesler, J. S. Guo, D. A. B. Iozzo, I. Legred, D. Li, S. Ma, D. Melchor, M. Morales, E. R. Most, M. A. Pajkos, T. Ramirez, N. Ring, H. R. Rüter, J. Sanchez, L. C. Stein, S. Thomas, D. Vieira, T. Wlodarczyk, and D. Wu, "Spectre," (2023).

[106] SXS, "paper-2023-spectre-enthalpy-eos," https://github.com/sxs-collaboration/paper-2023-spectre-enthalpy-eos (2023).

[107] P. Virtanen, R. Gommers, T. E. Oliphant, M. Haberland, T. Reddy, D. Cournapeau, E. Burovski, P. Peterson, W. Weckesser, J. Bright, S. J. van der Walt, M. Brett, J. Wilson, K. J. Millman, N. Mayorov, A. R. J. Nelson, E. Jones, R. Kern, E. Larson, C. J. Carey, İ. Polat, Y. Feng, E. W. Moore, J. VanderPlas, D. Laxalde, J. Perktold, R. Cimrman, I. Henriksen, E. A. Quintero, C. R. Harris, A. M. Archibald, A. H. Ribeiro, F. Pedregosa, P. van Mulbregt, and SciPy 1.0 Contributors, Nature Methods **17**, 261 (2020).

[108] T. Oliphant, "NumPy: A guide to NumPy," USA: Trelgol Publishing (2006–), [Online; accessed ¡today¿].

[109] J. D. Hunter, Computing in Science & Engineering **9**, 90 (2007).

[110] U. Ayachit, *The ParaView Guide: A Parallel Visualization Application* (Kitware, Inc., Clifton Park, NY, USA, 2015).

[111] J. A. Font, T. Goodale, S. Iyer, M. A. Miller, L. Rezzolla, E. Seidel, N. Stergioulas, W.-M. Suen, and M. Tobias, Phys. Rev. D **65**, 084024 (2002), arXiv:gr-qc/0110047.